



Geochemistry, Geophysics, Geosystems

RESEARCH ARTICLE

10.1029/2019GC008771

This article is a companion to Royden and Holt (2020), <https://doi.org/10.1029/2020GC009032>.

Key Points:

- By linking dip to mantle pressure via a force balance, we investigate global mantle flow as constrained by the Earth's slab dip distribution
- Models produce pressure fields consistent with Earth dips when material is down fluxed into the lower mantle on the upper plate side of slabs
- Slab dips provide a constraint on dynamic pressure patterns in the upper mantle

Supporting Information:

- Supporting Information S1

Correspondence to:

A. F. Holt,
aholt@miami.edu

Citation:

Holt, A. F., & Royden, L. H. (2020). Subduction dynamics and mantle pressure: 2. Towards a global understanding of slab dip and upper mantle circulation. *Geochemistry, Geophysics, Geosystems*, 20, e2019GC008771. <https://doi.org/10.1029/2019GC008771>

Received 17 OCT 2019

Accepted 6 MAY 2020

Accepted article online 16 MAY 2020

Subduction Dynamics and Mantle Pressure: 2. Towards a Global Understanding of Slab Dip and Upper Mantle Circulation

Adam F. Holt^{1,2} and Leigh H. Royden¹

¹Department of Earth, Atmospheric, and Planetary Sciences, MIT, Cambridge, MA, USA, ²Rosenstiel School of Marine and Atmospheric Sciences, University of Miami, Miami, FL, USA

Abstract We investigate the relationship between the global distribution of deep slab dips (at 250- to 300-km depth) and pressure and circulation in the upper mantle. Using an analytic method to compute dynamic pressure in a 3-D global upper mantle domain, and a force balance between slab dip, slab buoyancy, and pressure, we model dips for all major subduction zones. Overall, our models suggest that global-scale mantle flow, as dictated by the shapes and velocities of Earth's plates and slabs, plays a fundamental role in creating the global pattern of slab dips. The dip trends of the South American and western Pacific subduction zones are controlled, in our models, by spatial variations in the dynamic pressure associated with flow. Our best fitting models produce global root mean square dip misfits of less than 10° for asthenospheric viscosities of $2.5\text{--}4.0 \times 10^{20}$ Pas. This result is only obtained with a large flux of asthenosphere from upper to lower mantle at subduction boundaries, occurring on the overriding plate side of slabs, without which dips are significantly steeper than observed. This effect cannot be resolved by processes that affect only certain subduction systems and requires flux of asthenosphere into the lower mantle at subduction systems globally (or an alternative mechanism that produces more negative pressures on the overriding plate side of slabs). Upper mantle pressure fields that fit global slab dips yield negative dynamic pressure on the upper plate side of slabs, positive pressure on the subducting plate side, and an east-to-west pressure increase beneath the Pacific Plate.

1. Introduction

The subduction of a negatively buoyant lithospheric plate below an overriding plate and into the sub-lithospheric mantle is one of the fundamental components of plate tectonics. An abundance of regional subduction modeling studies has made advances in isolating the subduction properties and parameters needed to replicate many subduction zone observables (e.g., plate and trench motions, slab dips, topography, and lithospheric stress state). For example, the strength of subducting slabs (e.g., Becker et al., 1999; Bellahsen et al., 2005; Enns et al., 2005; Ribe, 2010), overriding plate properties (e.g., Capitanio et al., 2010; Holt, Becker et al., 2015; Sharples et al., 2014; Yamato et al., 2009), and three dimensionality of subduction zones (e.g., Piromallo et al., 2006; Schellart et al., 2007; Stegman et al., 2006) have all been shown to strongly affect subduction dynamics. However despite these insights, the processes that control deep slab dip are unclear, and an explanation for the global distribution of dips remains a major geodynamic goal.

Instantaneous mantle flow calculations have shown that high-density, high-viscosity subducting slabs are needed to reproduce Earth's plate motions and geoid (e.g., Becker & O'Connell, 2001; Hager, 1984; Lithgow-Bertelloni & Richards, 1998; Ricard & Vigny, 1989). Furthermore, global studies with more complex visco-plastic lithospheric rheologies have demonstrated that Earth-like subduction zones can emerge self-consistently in dynamic models of mantle convection (e.g., Crameri & Tackley, 2014; Mallard et al., 2016). However, only relatively few studies have focused on the degree to which the global distribution of current subduction observables—for example, slab dip and trench motion—may be a product of mantle flow on a global scale (e.g., Alisic et al., 2012; Hager & O'Connell, 1978; Husson, 2012). Methodological difficulties in incorporating regional subduction dynamics into a global framework are partly responsible for the limited work on this topic, as resolving “Earth-like,” present day subduction zones requires numerical simulations that are often extremely expensive (e.g., Alisic et al., 2012; Stadler et al., 2010).

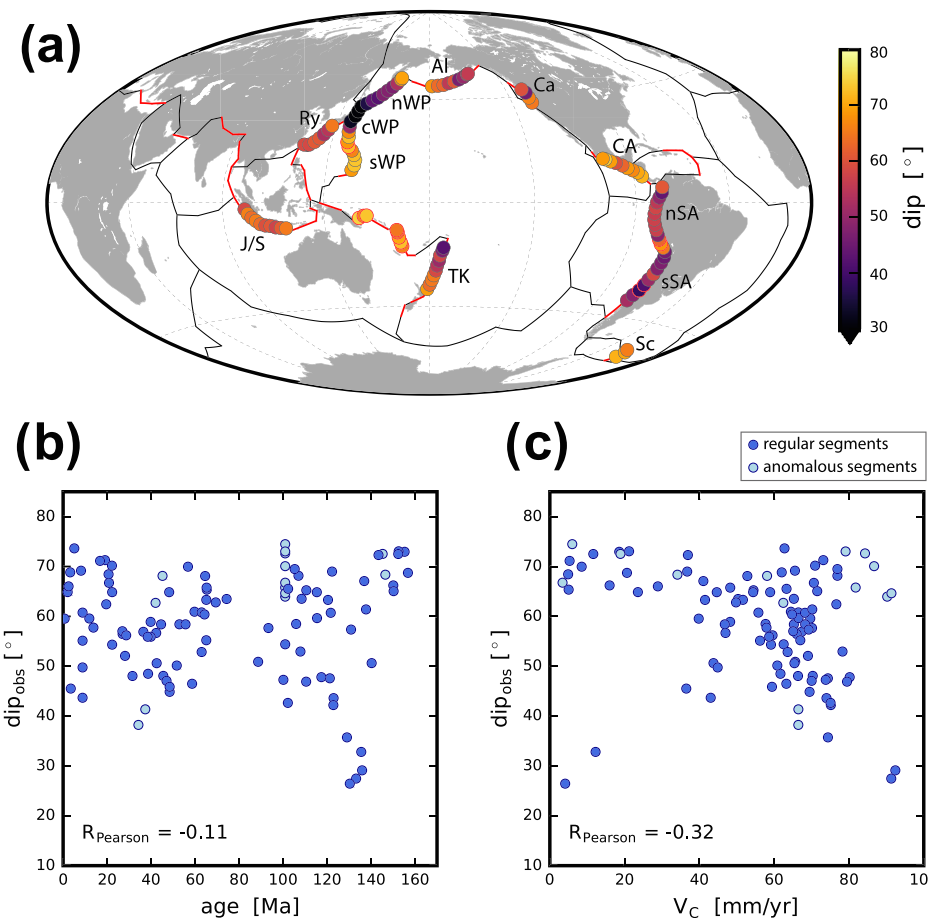


Figure 1. (a) Global slab dips extracted from Slab2.0 (Hayes et al., 2018) at depths of 300 km (or greatest depths available if slab is shallower than 300 km). (b) Slab dip versus subducting plate age extracted at a distance of 225-km outboard of the trench (Müller et al., 2008). (c) Slab dip versus subduction zone convergence rate (Lallemand et al., 2005). Labeled are the subduction zones analyzed in subsequent figures: J/S = Java/Sunda, Ry = Ryukyu, sWP = southern western Pacific (latitude < 32°N), cWP = central western Pacific (32°N < latitude < 44°N), nWP = northern western Pacific (latitude > 44°N), Al = Aleutian, Ca = Cascadia, CA = Central America, nSA = northern South America (latitude > 17°S), sSA = southern South America (latitude < 17°S), Sc = scotia. Dip angles of complicated subduction segments (continental/ridge/plateau subduction), which are omitted from subsequent analysis (and the correlation coefficient calculation), are outlined in red on the map and colored lighter blue on the scatter plots.

Mantle flow computations that do not explicitly resolve subduction zones, and are therefore less computationally expensive, generally use postprocessing force balances to determine how the slabs would behave within the computed flow field (e.g., Hager & O'Connell, 1978; Husson, 2012). While their approach treats only the effect of mantle flow on subduction zones (and not vice versa), it nonetheless suggests that subduction zones are strongly sensitive to their location within the global mantle circulation. For example, Hager and O'Connell (1978) showed that slab Benioff zones align broadly with the mantle velocity vectors of a plate motion-driven mantle circulation computation, which suggests a link between the forces associated with large-scale mantle flow and slab dip.

Deep slab dips (~300-km depth) do not appear to correlate strongly with regional subduction parameters (e.g., Cruciani et al., 2005; Jarrard, 1986; Lallemand et al., 2005); there is no deep slab dip correlation with slab age (buoyancy) (Figure 1b) and a relatively minor correlation with convergence rate (Figure 1c) and absolute upper plate velocity. Interestingly, shallow slab dips exhibit an inverse correlation with subduction duration (Hu & Gurnis, 2020; Jarrard, 1986) and overriding plate thickness/type (e.g., Holt, Buffett et al., 2015; Hu & Gurnis, 2020), but these correlations do not persist to the deep slab depths considered here. It is therefore reasonable to ask whether global-scale mantle flow plays a significant role in controlling deep

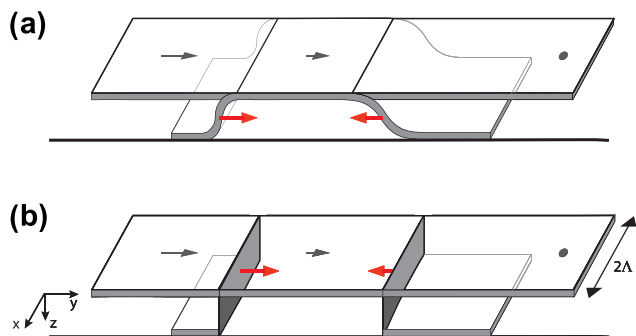


Figure 2. Schematic showing how geometries for subducting slabs (a) are idealized as rigid vertical “slab walls,” which are equivalent to an infinite viscosity barrier (b). The horizontal velocity of each slab wall is set equal to that of the corresponding slab profile.

mantle and, in turn, slab dips. We begin with flow that is constrained within the upper mantle and exhibits asthenospheric counter flow (e.g., Harper, 1978; Parmentier & Oliver, 1979; Schubert et al., 1978) and later consider the effects of material transfer from the upper to the lower mantle at subduction zones. In addition to understanding how mantle flow, and the resulting dynamic pressure field, controls the global distribution of slab dips, our ultimate goal is to explore the use of deep slab dips as probes of Earth’s global mantle pressure field.

2. Dynamic Pressure and Flow in the Upper Mantle: A Hele-Shaw Approach

Flow in Earth’s upper mantle must be dynamically consistent with the motions of the plates and the lateral motion of slabs. By prescribing plate and slab motions, we neglect the driving forces of these motions, generally considered to be the negative buoyancy of the slabs, and do not consider nonslab buoyancy and viscosity anomalies. While these approximations are significant, we choose to simplify the system in this way in order to develop analytical expressions and, in turn, target first-order understanding of the linkage between slab dips and upper mantle flow.

The approach presented in this paper builds on a companion paper that develops the analytical method in a Cartesian domain, explores the dynamics of some illustrative subduction scenarios, and compares the analytically computed pressure and velocity fields with those computed numerically (Royden & Holt, 2020). In this paper, we extend this methodology to spherical shell (global upper mantle) domains in order to explore the upper mantle pressure fields consistent with Earth’s plate and slab geometry and motions.

We follow Royden and Husson (2006) in dividing the full 3-D problem of asthenospheric flow into two coupled components: (1) a regional—or global—flow solution that describes upper mantle flow except within the upper, mantle wedge region and (2) a local flow solution near the slab region (i.e., “corner” or “wedge flow”) that adds an additional component of dynamic pressure. For our pressure calculations, we consider only the regional pressure solution in our analytical models. This is a reasonable approach because, at the ~300-km depths that we compute model dips, the dynamic pressure associated with wedge flow is negligible relative to the dynamic pressures induced by the larger-scale, regional flow (e.g., Stevenson & Turner, 1977; Tovish et al., 1978).

Following Royden and Holt (2020), a Hele-Shaw type of approximation is used to solve for the dynamic pressure field associated with flow in a thin viscous channel. We compute the upper mantle pressures and asthenospheric velocities that are consistent with a priori specified trench and plate geometries and velocities. In our models, we replace all slabs by rigid vertical walls at the location where the slabs pass through the mid-depth of the asthenospheric channel (i.e., 330 km; Figure 2). Each of these “slab walls” moves horizontally at the velocity of the corresponding slab profile (equal to trench velocity if slab dip is constant through time).

slab dip. Our previous numerical modeling indicates that slab dip embodies a local interplay between slab buoyancy and viscous mantle flow (Holt et al., 2017, 2018). These studies indicate that deep slab dip is a product of the pressure field surrounding the slab via a force balance that equates the subducting plate’s negative buoyancy to the difference in dynamic across the slab. Thus, slab dip is strongly and predictably affected by the dynamic pressure in the mantle, which is in turn a product of the large-scale flow regime in the mantle.

In this paper, we therefore investigate the degree to which the global distribution of slab dips (Figure 1a) may be a product of the Earth’s global mantle flow regime. In a companion paper (Royden & Holt, 2020), we have shown that obstruction of mantle flow by slabs produces asymmetry in the dynamic pressure fields that surround subducting slabs. In particular, across-slab discontinuities in dynamic pressure arise from such obstruction, and these discontinuities can be converted to model slab dips. Using a similar modeling technique, this paper explores how Earth’s global configuration of plate and slabs controls the pressure field in the upper

The kinematic requirements on the system are that the horizontal velocity at the upper surface of the asthenosphere is equal to that of the overlying, rigid plate and that asthenosphere adjacent to the slab walls flows in the correct direction. Adjacent to each slab wall, the slab-normal velocity of the asthenosphere must be equal to that of the horizontal velocity of the slab wall. In the first set of models in this paper, we assume that there is no flux of asthenosphere between upper and lower mantle. In the second set of models, we assume that downward flux of asthenosphere into the lower mantle occurs only along a narrow zone adjacent to the slabs. To preserve the volume of the asthenosphere in these downward flux models, we counterbalance this with an upward flux distributed uniformly over the entire asthenosphere lower mantle interface.

To avoid cumbersome terminology, we will refer to the upper mantle, excluding plates and slabs, as “asthenosphere.” “Pressure” refers dynamic pressure, determined from total pressure by subtracting from it the pressure at an equivalent depth in a hydrostatic column of asthenosphere beneath a mid-ocean ridge.

2.1. Fundamental Equations

We begin by defining the asthenosphere as a thin spherical annulus with outer radius R (6,370 km) and thickness a (580 km), overlain by an 80-km thick rigid plates. We define a spherical coordinate system as coordinates r (radius), θ (polar angle), and φ (azimuthal angle). In the Hele-Shaw approximation (e.g., Batchelor, 2000), shear and deviatoric stresses on vertical surfaces are neglected. Force balances in the θ and φ directions then yield:

$$\frac{1}{r^2} \frac{\partial}{\partial r} (r^2 \tau_{r\theta}) = \frac{1}{r} \frac{\partial P}{\partial \theta} \quad \frac{1}{r^2} \frac{\partial}{\partial r} (r^2 \tau_{r\varphi}) = \frac{1}{r} \frac{\partial P}{\partial \varphi}, \quad (1)$$

where P is dynamic pressure and τ is shear stress on planes of constant r . These can be combined with expressions relating shear stress to tangential velocity:

$$\tau_{r\theta} = r\mu \frac{\partial}{\partial r} \left(\frac{v_\theta}{r} \right) \quad \tau_{r\varphi} = \frac{r\mu}{\sin(\theta)} \frac{\partial}{\partial r} \left(\frac{v_\varphi}{r} \right). \quad (2)$$

Combining to obtain v_θ yields:

$$v_\theta = r \int_r^R \frac{dr}{\mu r^3} \int_r^R r \frac{\partial P}{\partial \theta} dr + c_{1\theta} r \int_r^R \frac{dr}{r^3 \mu} + c_{2\theta} \left(\frac{r}{R} \right), \quad (3)$$

where $c_{1\theta}$ and $c_{2\theta}$ are constants of integration.

The dependence of pressure on depth can be assessed by requiring that in the limit where R becomes indefinitely large compared to a , the relationship between tangential velocity and dynamic pressure reduces to the Cartesian result for Hele-Shaw flow. This holds only when P scales inversely with r . Computing v_φ in the same manner as v_θ (Equation 3), and using a plate velocity \mathbf{v}_p , a uniform viscosity (μ) and thickness (a) for the asthenosphere, and a stress-free (free slip) lower boundary condition, the expression for tangential velocity, \mathbf{v}_a , becomes:

$$\mathbf{v}_a = \frac{\nabla P_R}{2\mu} \left(\frac{R^3 - aR^2}{r} + rR + ar - 2R^2 \right) + \mathbf{v}_p \left(\frac{r}{R} \right), \quad (4)$$

where P_R is pressure at the outer channel radius and boldface indicates vector quantities. The velocity expression in Equation 4 contains a “pressure-driven” component that is linearly proportional to ∇P_R , which has zero velocity at the top of the channel and zero shear stress at the base of the channel. It also contains a “plate-driven” component of flow that has a velocity equal to \mathbf{v}_p at the top of the channel and zero shear stress at all depth.

Because a is much lesser than R , it is convenient to substitute $r = R - z$, where z is depth relative to the outer surface of the channel. A Taylor series expansion for $1/r = 1/(R - z)$ gives:

$$\mathbf{v}_a = \left[\frac{\nabla P_R}{\mu} \left(\frac{z^2}{2} - za \right) + \mathbf{v}_p \right] + \left[\frac{\nabla P_R}{\mu} \left(\frac{z^3 - az^2}{2R} \right) - \mathbf{v}_p(z/R) \right]. \quad (5)$$

The term in the first set of square brackets are the same as those for flow in a planar channel (e.g., Royden & Holt, 2020). Terms in the second set of square brackets, of order a/R , are attributable to the spherical geometry. Higher-order terms in a/R have been omitted (yielding errors of less than ~1% for flow in a spherical annulus with a geometry equivalent to Earth's upper mantle).

The vertically averaged velocity within the asthenosphere is obtained by integrating Equation 5 over asthenospheric depths and dividing by a :

$$\bar{\mathbf{v}}_a = -\frac{\nabla P_R a^2}{\mu} \left(1 + \frac{a}{8R} \right) + \mathbf{v}_p \left(1 - \frac{a}{2R} \right). \quad (6)$$

Similarly, the vertically averaged velocity throughout the entire upper mantle, including the lithosphere is

$$\bar{\mathbf{v}}_{\text{total}} = -\frac{\nabla P_R a^3}{\mu} \left(1 + \frac{a}{8R} \right) + \mathbf{v}_p \left(1 - \frac{a^2}{2Rh} \right), \quad (7)$$

where h is the total thickness of the upper mantle (660 km). See the supporting information for the derivation of equivalent expressions for the case of no-slip lower boundary condition (supporting information Section S1).

In addition to exploring the dynamics of flow constrained to the upper mantle, we want to allow for possible flux of asthenosphere into the lower mantle (localized at subduction zones). If the total volume rate of flux summed over all subduction zones, F_{net} , is compensated by evenly distributed, upwards flow from the lower mantle into the asthenosphere, then we can take the divergence of Equation 7 to find:

$$\frac{F_{\text{net}}}{4\pi(R-a)^2} = -\nabla^2 P_R \left[\frac{a^3}{3\mu h} \left(1 + \frac{a}{8R} \right) \right] + \nabla \cdot \mathbf{v}_p \left(1 - \frac{a^2}{2Rh} \right), \quad (8)$$

where we note that the divergence of \mathbf{v}_p is zero except at plate boundaries (note that other distributions of flow through the base of the asthenosphere can be obtained by substituting F_{net} with a flux distribution that is dependent on position).

2.2. Analytic Solutions for Dynamic Pressure

In order to derive solutions to Equation 8 for Earth-like plate and slab geometries, we begin by dividing all plate boundaries into short, great-circle segments. As described in detail in Royden and Holt (2020), breaking up plate boundaries into smaller segments—each with their own pressure solution components—enables us to develop solutions for networks of plates and plate boundaries with arbitrarily complex geometries.

To solve for dynamic pressure and flow in a Cartesian domain, Royden and Holt (2020) employ two types of pressure solutions: edge (P_{edge}) and wall solutions (P_{wall}). Edge solutions are associated with all plate boundary segments at sites of relative plate motion (i.e., all active plate boundaries), while wall solutions are only associated with subduction zones (i.e., slab walls). For volume conservation, the coefficients of these solutions, explained in more detail in section 2.3, enforce that the net flow of asthenosphere be equal on either side of each nonslab plate boundary. Unless there is downward flux of asthenosphere into the lower mantle adjacent to slabs, we also require that the slab-normal velocity of asthenosphere adjacent to the slab wall be equal to that of the slab wall. Here, we derive highly accurate spherical approximations to these functions because exact solutions in a spherical domain are difficult to derive and mathematically cumbersome.

The first of these functional forms is P_{edge} . These functions produce a boundary-normal component of velocity that is equal and opposite on either side of the plate boundary segment and is continuous elsewhere. The associated dynamic pressure is continuous everywhere. P_{edge} functions are needed to compensate for the discontinuity in velocity produced by the “plate-driven” component of flow at plate boundaries. That is,

P_{edge} functions centered about each plate boundary segment, and properly scaled, provide continuity of flow across the boundary.

For planar flow (i.e., in a Cartesian domain), the function $P_{\text{edge}}^{\text{planar}}$ that corresponds to a plate boundary segment of length 2Λ is:

$$P_{\text{edge}}^{\text{planar}}(D, \phi) = A\Lambda \left(\frac{3\mu}{a^2} \right) \left\{ D' \frac{\sin(\phi)}{\pi} \left[\tan^{-1} \left(\frac{D'\cos(\phi) - 1}{D'\sin(\phi)} \right) - \tan^{-1} \left(\frac{D'\cos(\phi) + 1}{D'\sin(\phi)} \right) \right] - \left(\frac{1 + D'\cos(\phi)}{2\pi} \right) \ln(D'^2 + 2D'\cos(\phi) + 1) + \left(\frac{D'\cos(\phi) - 1}{2\pi} \right) \ln(D'^2 - 2D'\cos(\phi) + 1) \right\}, \quad (9)$$

where A is a constant with units of velocity, $\left(\frac{3\mu}{a^2} \right)$ is the “viscosity coefficient” associated with a free-slip base and uniform viscosity asthenosphere, D is distance from the center of the plate boundary segment, $D' = D/\Lambda$, and ϕ is azimuthal angle, with $\phi = 0$ being parallel to the plate boundary segment (Royden & Holt, 2020).

For flow in a spherical shell, the Cartesian form of $P_{\text{edge}}^{\text{planar}}(D, \phi)$ provides a good approximation for dynamic pressure and velocity near the plate boundary segment about which it is centered but is a poor approximation far from the plate boundary segment. We therefore modify this expression to provide a good approximate solution for dynamic pressure far from the plate boundary segment by subtracting and adding “monopole” solutions in Cartesian and spherical domains, respectively.

The planar “monopole” solution, $P_{\text{monopole}}^{\text{planar}}$, is obtained by taking the limit of Equation 9 as the length of the segment (Λ) goes to zero, while keeping the product $A\Lambda$ constant:

$$P_{\text{monopole}}^{\text{planar}}(D) = -\frac{2A\Lambda}{\pi} \left(\frac{3\mu}{a^2} \right) \left\{ 1 + \ln \left(\frac{D}{\Lambda} \right) \right\}. \quad (10)$$

At large distances from the plate boundary segment $P_{\text{monopole}}^{\text{planar}}$ becomes equal to $P_{\text{edge}}^{\text{planar}}$. We compute the spherical monopole solution scaled such that it becomes equal to this planar monopole as D becomes small:

$$P_{\text{monopole}}^{\text{sphere}}(D) = -\frac{A\Lambda}{\pi} \left(\frac{3\mu}{a^2} \right) \left[\ln \left(1 - \cos \left(\frac{D}{R} \right) \right) - \ln \left(\frac{\Lambda^2}{2R^2} \right) + 2 \right]. \quad (11)$$

Combining all three components yields an approximate expression for dynamic pressure in a spherical annulus.

$$P_{\text{edge}}^{\text{sphere}}(D, \phi) = P_{\text{edge}}^{\text{planar}}(D, \phi) - P_{\text{monopole}}^{\text{planar}}(D) + P_{\text{monopole}}^{\text{sphere}}(D). \quad (12)$$

The last two terms on the right side of Equation 12 cancel near the plate boundary segment about which $P_{\text{edge}}^{\text{sphere}}$ is centered; here, the pressure and velocity reduce to a Cartesian solution for flow near that plate boundary segment. Far from the plate boundary segment, the first two terms on the right cancel, and the solution becomes that of the spherical monopole, which is what we expect for an exact solution for $P_{\text{edge}}^{\text{sphere}}$ at large distance from the plate boundary segment. As in the Cartesian case, the boundary-normal components of velocity associated with $P_{\text{edge}}^{\text{sphere}}$ are equal in magnitude and opposite in sign on either side of the boundary.

While the Laplacian of $P_{\text{edge}}^{\text{planar}}$ (and the divergence of the associated, vertically averaged velocities) is zero, which corresponds to mass conservation, the Laplacian of $P_{\text{monopole}}^{\text{sphere}}$ (and hence $P_{\text{edge}}^{\text{sphere}}$) is a nonzero constant. If there is no flow in or out of the lower mantle, then the sum of all these $P_{\text{monopole}}^{\text{sphere}}$ and $P_{\text{edge}}^{\text{sphere}}$ terms, one centered at each plate boundary segment, will have a Laplacian of zero, as follows from Equation 8 (because the divergence of the plate velocities, integrated over the surface of the sphere, must be zero to ensure mass continuity). If there is a net flow of asthenosphere into the lower mantle, for example, at subduction

boundaries, the sum of the Laplacians will be a constant related to the rate of compensating upward flow. The location of the compensating upward flow can be chosen as desired. In this paper, we do not specify a distribution for this upward flow, which results in its automatic uniform distribution over the entire base of the asthenosphere.

The second useful functional form for dynamic pressure in a Cartesian domain, $P_{\text{wall}}^{\text{planar}}$, produces asthenospheric velocities whose boundary-normal components are equal in magnitude and sign on either side of a linear plate boundary segment. These solutions display a pressure field that is discontinuous across the plate boundary segment and so are only used at subduction zones where a slab, idealized as a vertical slab wall, separates the asthenosphere on either side of the wall (Figure 2). Solutions of this form are responsible for the asymmetry in the pressure field on either side of a slab wall (Royden & Holt, 2020).

To derive a spherical equivalent, we proceed as above, beginning with the solution for planar flow:

$$P_{\text{wall}}^{\text{planar}}(D, \phi) = B\Lambda \left(\frac{3\mu}{a^2} \right) \left\{ -D \sin(\phi) + \frac{1}{\sqrt{2}} \frac{|\sin(\phi)|}{\sin(\phi)} \sqrt{1 - D'^2 \cos^2(\phi) + D'^2 \sin^2(\phi) + \sqrt{(D'^2 + 1)^2 - 4D'^2 \cos^2(\phi)}} \right\}, \quad (13)$$

where B is a constant with units of velocity. As for the edge solution, this provides an excellent approximation for dynamic pressure and velocity near the plate boundary segment but is a poor approximation far from the plate boundary segment.

In order to provide a good approximate solution for dynamic pressure far from the plate boundary segment, we modify this expression using a similar strategy as that adopted for the edge solutions. In this case, however, we subtract and add “dipole” solutions for Cartesian and spherical domains. The planar dipole solution, $P_{\text{dipole}}^{\text{planar}}$, is derived by taking the limit of Equation 13 as Λ goes to zero, while keeping the product $B\Lambda^2$ constant:

$$P_{\text{dipole}}^{\text{planar}}(D, \phi) = \left(\frac{3\mu}{a^2} \right) \left(\frac{B\Lambda^2}{2D} \right) \sin(\phi). \quad (14)$$

At large distances from the plate boundary segment, $P_{\text{dipole}}^{\text{planar}}$ becomes equal to $P_{\text{wall}}^{\text{planar}}$. We also compute the spherical dipole solution, scaled so that it becomes equal to the planar dipole as D becomes small:

$$P_{\text{dipole}}^{\text{sphere}}(D, \phi) = \left(\frac{3\mu}{a^2} \right) \left(\frac{B\Lambda^2}{4R} \right) \left(\frac{\sin(\phi) \sin\left(\frac{D}{R}\right)}{1 - \cos\left(\frac{D}{R}\right)} \right). \quad (15)$$

Following the methodology used to derive $P_{\text{edge}}^{\text{sphere}}$, we combine all three components to obtain an approximate expression for dynamic pressure in a spherical annulus.

$$P_{\text{wall}}^{\text{sphere}}(D, \phi) = P_{\text{wall}}^{\text{planar}}(D, \phi) - P_{\text{dipole}}^{\text{planar}}(D, \phi) + P_{\text{dipole}}^{\text{sphere}}(D, \phi). \quad (16)$$

The Laplacian of $P_{\text{dipole}}^{\text{sphere}}$ is zero everywhere, except along the plate boundary segment, and so $P_{\text{wall}}^{\text{sphere}}$ is not a source-sink term but rather works to impose a barrier to asthenospheric flow at slab boundaries. It is only the $P_{\text{wall}}^{\text{sphere}}$ terms that create asymmetric dynamic pressure across the slab barrier.

In the supporting information (Figure S1 and Section S2), we show that the error in these spherical approximations is less than a small fraction of a percent for $\Lambda \leq 0.1R$ and smaller than other potential sources of error, such as those associated with the Taylor series approximation of Equation 4 and those inherent in

this application of the Hele-Shaw method (see Royden & Holt, 2020, for detailed discussion and comparison with numerical solutions).

2.3. Summation of Solutions for Multi-segment Systems

We divide each plate boundary without a subduction zone into great circle segments 200 km in length and each plate boundary with a subduction zone into great circle segments 100 km in length. Figure S1 shows convergence tests that justify the use of these segment lengths. Within the matrix calculation that we use to calculate the coefficients of the pressure solutions, each of these plate boundary segments is associated with a function $A_n P_{\text{edge}}^{\text{sphere}}$ and a function $B_n P_{\text{wall}}^{\text{sphere}}$, centered on that segment, where A_n and B_n are constants. However, B_n is zero if the n th segment is not along a subduction boundary (i.e., nonsubduction boundaries do not contain slab walls). The global pressure field, determined at the upper surface of the viscous channel, is then represented by N wall and edge functions weighted by the coefficients A_n and B_n :

$$P_R(D, \phi) = \sum_{n=1}^N A_n P_{\text{edge}}^{\text{sphere}}(D_n, \phi_n) + \sum_{n=1}^N B_n P_{\text{wall}}^{\text{sphere}}(D_n, \phi_n), \quad (17)$$

where N is the total number of segments. D_n and ϕ_n are the great-circle distance and azimuthal angle of point (D, ϕ) relative to the center of the n th plate boundary segment (with $\phi_n = 0$ lying along, or parallel to, the n th boundary segment).

The coefficients (A_n, B_n) in this expression are determined simultaneously by matrix inversion. The constraints on the inversion are velocity constraints at all plate boundary segments (e.g., Equations 6 and 7). For segments without slabs, the boundary-normal component of velocity is required to be equal on both sides of the boundary. For segments with slabs, the boundary-normal component of velocity on both sides of the slab wall is set to the slab wall velocity (or to a velocity modified to account for flux of asthenosphere into the lower mantle at that segment boundary; section 6.2). For a system with N plate boundary segments, containing M segments that lie along slab boundaries, this yields a linear system of $N+M$ equations, corresponding to square matrix of dimension $N+M$.

The Python code necessary to conduct computations of subduction-induced upper mantle flow for user-specified plate and slab geometries is available in the following repository: <https://doi.org/10.5281/zenodo.3774385>. This includes the main analytical flow code, the reference plate and slab geometry, Earth dips derived from Slab2 (Section 4.1.2), and the postprocessing scripts needed to convert modeled pressure fields into modeled slab dips (Section 6).

3. Idealized Subduction Geometries

Before proceeding to models with Earth-like plate and slab geometries, we present idealized models containing simple plate geometries. This illustrates the basic relationships between subduction geometry and dynamic pressure in the mantle. Of particular importance is the dynamic pressure difference across subducting slabs, ΔP , which exerts a direct control on slab dip. In these examples, and later in the paper, we compute values of ΔP at mid-upper mantle depth (330 km). For these simple examples, we use a viscosity of 3×10^{20} Pas. Because dynamic pressure in a Newtonian fluid scales linearly with viscosity, the resulting pressures can be simply scaled up or down for different values of viscosity. In all models, the dynamic pressure field is constrained to have an average pressure of zero on the surface of the asthenospheric channel, where we assume a uniform, 80-km plate thickness.

Consider a small, Nazca-sized, plate ($5,000 \times 5,000$ km), moving westward at an equatorial velocity of 5 cm/year relative to the larger stationary plate that makes up the remainder of the system (Figure 3). This produces a convergent margin at the plate's western boundary and a spreading ridge at the plate's eastern boundary. The convergent margin is represented as a slab wall that "retreats" east with an equatorial velocity of 5 cm/year. The pressure field generated in this example develops positive dynamic pressures as high as 17 MPa behind (on the subducting plate side) the moving slab and negative pressure as low as -7 MPa in front (on the upper plate side) of the slab (Figure 3a). The magnitude of the discontinuity in dynamic pressure across the slab, ΔP , is a maximum of 24 MPa in the central slab region. This pressure

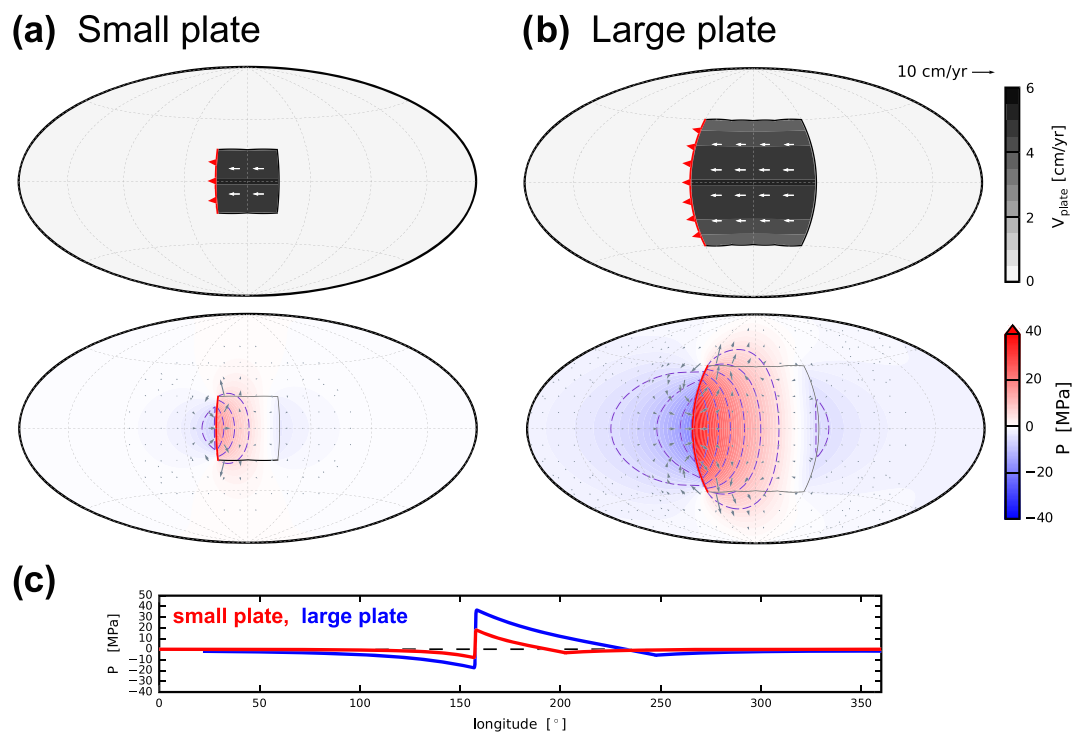


Figure 3. Global upper mantle pressure computations for two idealized geometries: (a) A small plate with a retreating trench ($5,000 \times 5,000$ km), and (b) a large plate with a retreating trench ($10,000 \times 10,000$ km). Both models have a mantle viscosity 3×10^{20} Pas. For each model, we show the imposed plate velocities, wall locations (red), computed upper mantle pressure field (5 MPa interval contours overlain), and average upper mantle velocity field (gray vectors). The slab wall retreats at 5 cm/year (eastwards) and the subducting plate moves westwards at ≈ 5 cm/year (Euler pole at the north pole with a $0.45^\circ/\text{Myr}$ rotation). Panel (c) compares equatorial pressure profiles for the two models.

distribution is associated with the canonical subduction-induced flow around the slab, accommodating the slab's retreating motion and ensuring mass conservation (e.g., Funiciello et al., 2003).

For a larger, approximately Pacific-sized plate ($10,000 \times 10,000$ km), a similar pattern develops but with much greater dynamic pressure magnitudes. Positive dynamic pressures as high as 36 MPa develop behind the slab and negative pressures as low as -17 MPa develop in front of the slab (Figure 3b). A maximum ΔP of 53 MPa develops in the central slab region, which illustrates the strong dependence of pressure magnitude on plate size, as explored extensively in a Cartesian domain by Royden and Holt (2020). As discussed in Section 4 (Equation 18), the higher magnitude ΔP in this large plate case corresponds to a significantly lower slab dip (e.g., $\sim 55^\circ$ for a 100 Myr old subducting plate) than the low magnitude ΔP in the small plate case (e.g., $\sim 75^\circ$ for a 100 Myr plate).

In addition to the size of the plate and length of the slab, the continuity and shape of the subducting slab exert a strong control on the mantle pressure field. The two models in Figure 4 illustrate how discontinuities or “slab gaps” and nonlinear slab shapes can modify the dynamic pressure field. A gap within the retreating slab wall provides an additional route for material to flow from one side of the slab to the other, thereby reducing the volume of material that flows around the ends of the slab. This decreases the overall magnitude of the dynamic pressure field and the magnitude of ΔP across the slab walls (cf. Figures 4a and 3b). Conversely, introducing a slab corner in the northwest traps mantle material behind the subducting plate and results in enhanced pressure build up and a greater magnitude ΔP across the slab walls (Figure 4b).

4. Earth Subduction Geometries

We now move to Earth-like geometries to investigate the interdependence of plate/slab geometry, global pressure distribution, and the pressure differences (ΔP) across slabs. In contrast to the rectangular-shaped

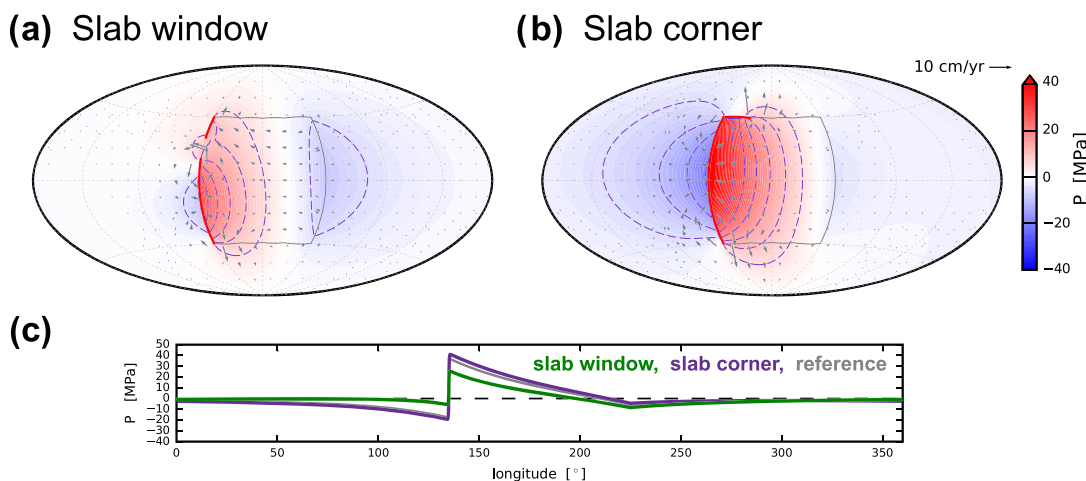


Figure 4. Global upper mantle pressure computations for two additional plate geometries. As in Figure 3b, both models have a “large plate” size, 5-cm/year retreating slab walls, and \approx 5-cm/year plate velocities to the west. Relative to Figure 3b, the models are modified by the addition of (a) a 1,650-km long gap in the trench/slab wall and (b) a stationary slab wall (1,950 km long) at the northwest boundary of the plate. Also displayed are the mantle pressure and velocity fields (a, b) and trench-perpendicular profiles of mantle pressure taken at the equator (c).

plate systems in Figures 3 and 4, Earth plates have complex shapes and a wide distribution of sizes and subduction zones that often curved and discontinuous.

4.1. Model Setup

In this section, we describe the global plate and slab geometry that we impose in our models, the slab dip catalog from which we determine observed dips, and our method for converting model pressure fields into model dips.

4.1.1. Model Plate and Slab Geometry

We construct a global subduction geometry using slab wall boundaries that are based on Slab2 (Hayes et al., 2018), a global model of three-dimensional slab geometry that utilizes hypocenter locations, seismic tomography, receiver functions, and other data types. We construct a reference slab geometry by placing vertical slab walls where Slab2 shows slab contours that extend to at least 150-km depth but neglect small subducting slabs within exceedingly complex tectonic regions such as parts of southeast Asia. In the supporting information, we present the full plate and slab geometry of our reference model and a range of model geometry perturbations (Figure S2). The slab walls are assumed to move at the same rate as the associated trench, with trench velocities taken from Heuret and Lallemand (2005) and Lallemand et al. (2005). Plate motions are from the MORVEL velocity model (Argus et al., 2011). Because we prescribe a free-slip model base, there is no inherent, absolute reference frame in our models and so the computation is independent of the frame chosen for the imposed plate and trench velocities (see also section 6.4 for tests with a no-slip lower boundary).

4.1.2. Slab Dip

Although slab dip is not explicitly contained in our analysis of dynamic pressure, we can relate slab dip to the dynamic pressure difference across the slab, ΔP , by requiring that ΔP supports the slab normal component of the buoyancy force acting on the slab at mid-asthenospheric depths. Or

$$(\Delta\rho gl)\cos(\theta) - \Delta P = 0, \quad (18)$$

where θ is the angle of slab dip and $\Delta\rho gl$ is the negative buoyancy of the slab per unit of down-dip slab length ($\Delta\rho$ is the average density difference between slab and asthenosphere, l is the thickness of the slab, and g is acceleration due gravity).

Pressures that are more positive beneath the subducting plate side of the slab and more negative beneath the overriding plate side of the slab are required to support negatively buoyant slabs at dips of less than 90° (e.g., Stevenson & Turner, 1977). In our sign convention, this corresponds to a positive ΔP . This relationship holds

for a wide range of numerically modeled 3-D subduction geometries (Figure 1 of Royden & Holt 2020), although bending stresses can play a role in slab support if the slab is significantly curved in the region where dip is measured.

For our dip “observations,” we use slab surfaces from Slab2, which have precomputed slab dips (Hayes et al., 2018) and separate major subduction zones into 250 long subduction segments. Most slab dips are extracted at 300-km depth. However, for major slabs that do not have well-defined dips at this depth, we extract the dip at the deepest available contour that extends along the full, trench-parallel length of the subduction zone, providing it is deeper than 200 km (see Figure S3 for further analysis of our slab dip catalog). Following Lallemand et al. (2005), we omit subduction segments that contain ridges, plateaus, or continental lithosphere from our observational dip catalog (Figure 1). Specifically, we do not consider the dips of subduction segments that are within 200 km of the Nazca and Juan Fernandez ridges (South America), within 200 km of the Ogasawara Plateau (Marianas), and continental subduction across the Tethyan and to the north of Australia. The resulting dip catalog has 93 segments with a mean dip of 57.5, a minimum dip of 26.5° (Japan), and a maximum dip of 73.6° (southern Mexico).

Because of resolution limitations inherent in imaging the mantle and locating earthquakes, and hence identifying slab surfaces, these “observed” dips have significant uncertainty. Lallemand et al. (2005) attribute an uncertainty of $\pm 5^\circ$ to their computed dips. Here, we estimate that the uncertainty derived from the Slab2 dips has been reduced to $\pm 2.5^\circ$ due to seismological developments and the consideration of a wider range of seismological datasets. We include this uncertainty as horizontal error bars in our model-observed dip comparison plots (e.g., Figure 5b).

4.1.3. Slab Buoyancy

For a given plate age, slab buoyancy ($\Delta\rho_{gl}$) can be computed from slab age by depth integrating the density anomaly associated with a half space cooling temperature profile. To do this, we assume a reference mantle density of $3,300 \text{ kg/m}^3$, a deep mantle-surface temperature contrast of 1,300 K, a thermal expansion coefficient of $3 \times 10^{-5} \text{ K}^{-1}$, and a thermal diffusivity of $10^6 \text{ m}^2/\text{s}$. At midmantle depths, positively buoyant basaltic crust has transformed to negatively buoyant eclogite and so we also include a 7.5-km thick $3,450 \text{ kg/m}^3$ of eclogite crust in our density integration (Lee & Chen, 2007). We extract subducting plate age from the global oceanic age grid of Müller et al. (2008), 225-km outboard of the midpoint of the relevant subduction segment, and assume that this is equivalent to the effective slab age at depth. In conjunction with the ΔP values computed in the models, these oceanic plate buoyancies can be used to derive model dips (Equation 18). Conversely, we can use the observed slab dip and the computed slab buoyancy to compute an “observed” ΔP across the slab.

5. Modeling the Western Pacific Slabs

We first apply our methodology to a simplified Earth system containing only the Pacific and Philippine Sea Plate boundaries and slabs. This is a good first test of the general approach because the observed dip of the Pacific slab varies from $\sim 30^\circ$ to $> 70^\circ$ along strike, while the buoyancy of the subducting slab changes relatively little. Hence, from the discussion of slab dip and dynamic pressure in section 4.1.2, one would expect large along-strike variations in the dynamic pressure difference across the Pacific slab.

For this plate and slab geometry, we find the best fitting (lowest RMS misfit) set of synthetic dips for a mantle viscosity of $7.9 \times 10^{20} \text{ Pas}$ (Figure 5a). Because dynamic pressure scales linearly with asthenospheric viscosity, this was determined by scaling the computed dynamic pressure using a range of asthenospheric viscosities, computing subduction segment dips for each viscosity value, and then determining which viscosity gives the lowest RMS misfit between observed and modeled dips. As shown in Figure 5a, the asthenospheric pressure in this model is strongly positive beneath the western Pacific and the Philippine Sea plates (40 to 70 MPa), mildly positive beneath Eurasia (~ 20 MPa), and highly negative at the East Pacific Rise (-40 to -60 MPa).

Figure 5b shows the corresponding “model” dips, calculated from the model ΔP values and our computed values for slab buoyancy (Equation 18 and section 4.1.3). For this model, the mean and RMS misfit between the observed and model dips are 5.6° and 6.6° , respectively, when dips are computed at every 250 km along the subduction zones (section 4.1.2). In the rest of the paper, we will refer to this type of RMS misfit as the

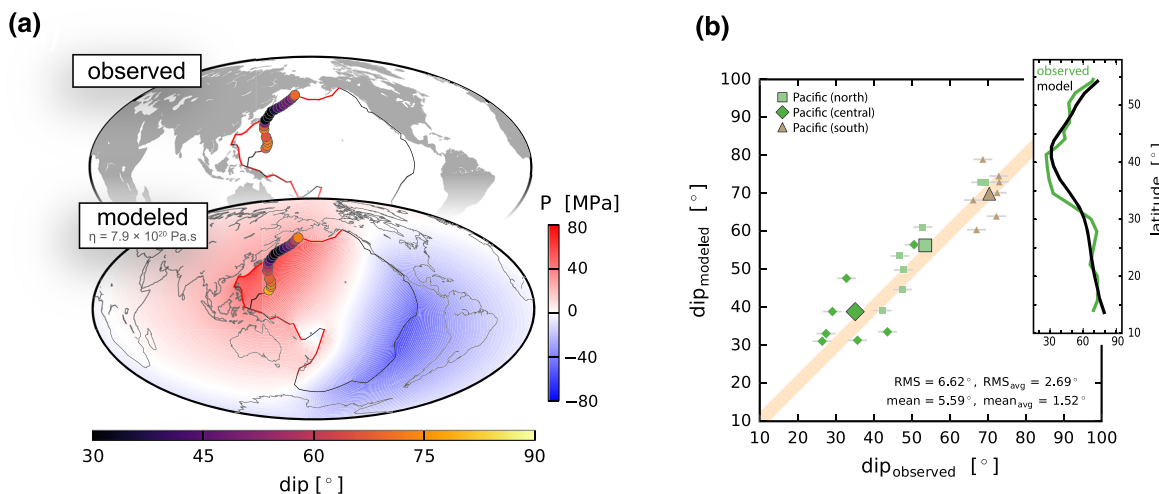


Figure 5. Comparison between observed and model slab dips in the Western Pacific. The model contains only the Pacific and Philippine Sea plates and has a mantle viscosity of 7.9×10^{20} Pas. Panels show (a) map view comparison of dips and model dynamic pressure field (330-km depth) and (b) along-strike profile and scatter plot comparisons of the modeled and observed dips. In the scatter plot, we also display dip values averaged over portions of the subduction zones, as larger symbols. The southern segment corresponds to latitude $< 32^\circ\text{N}$, central segment to $32^\circ\text{N} < \text{latitude} < 44^\circ\text{N}$, and northern segment to latitude $> 44^\circ\text{N}$.

“individual segment” misfit, where “segment” refers here to the segments used to calculate the dips (Figure 1a) and not the 100-km long plate boundary segments used in the analytical calculation (section 2.3). When averaged over three larger subduction domains (North, central, and southern Pacific), the mean and RMS misfits for dips are reduced to 2.7° and 1.5° , respectively. Although the observed dips show more fine-scale variation along strike, the model dips capture the along-strike trend well. Moreover, the method we have developed to determine asthenospheric pressure only captures features at horizontal scales greater than about half the channel thickness, or ~ 300 km, and would not be expected to replicate shorter length scale features.

The model slab dips replicate the extremely shallow dips ($30\text{--}40^\circ$) observed along the Japan subduction zone. These occur because Japan sits near the middle of the long subduction zone, where the highest pressures and pressure differences are found along continuous subduction systems (e.g., Figure 3). This effect is amplified by the curvature of the trench, which helps to confine asthenosphere on the eastern side of the slab wall, so that larger pressure gradients are needed to accommodate asthenospheric flow around the ends of the slab wall. To the north (Kamchatka) and south (Mariana), dips increase rapidly towards the ends of the slab wall. Hence, the first-order features of Pacific Plate slab dips are reconcilable by considering the kinked, large-scale geometry of the Western Pacific slabs. Because of the barrier to flow represented by the Philippine (Ryukyu) slab wall, elevated dynamic pressure beneath the Philippine Sea Plate also plays a role in controlling the slab dip along the Japan portion of the Pacific slab in this model (e.g., Holt et al., 2018).

Despite the excellent fit to observed dips along the Pacific slab, the best fit viscosity for the Pacific slab does not produce good agreement with the observed dip of the Ryukyu slab, under predicting it by $\sim 40^\circ$. If we choose instead to minimize the RMS misfit of both Ryukyu and Pacific slab dips, we find that a viscosity of 5.6×10^{20} Pas reduces the average Ryukyu misfit to $\sim 20^\circ$ but results in the over prediction of Pacific slab dips (Figure S4). However, we note that the Ryukyu slab is young (low negative buoyancy) and observed only to relatively shallow depths (~ 350 km) so that uncertainties associated with the buoyancy of the slab, and the assumption that the slab acts as a complete barrier to upper mantle flow, will have a proportionately large effect on the Ryukyu model dip. Also, the Philippine Sea Region is tectonically complex; it is difficult to define the slab boundaries along the southwestern margin of the plate, and the extent to which some of these young slabs extend to the base of the upper mantle is not always clear. (For example, removing the slab walls associated with the shallow Nankai and Philippine slabs, which significantly reduces positive pressure beneath the Philippine Sea Plate, is one possible way to concurrently match Pacific and Ryukyu slab dips;

Figure S4.) The behavior of the Ryukyu slab is discussed further in the context of the complete global system in section 6.

In the supporting information, we also examine the effect of including the presence of the Pacific “slab tail” at Japan latitudes (Figure S5). The slab tail is the portion of the subducting Pacific Plate that lies flat atop of the lower mantle (~670 km) and extends westwards along the transition for a lateral distance of more than 2,000 km (e.g., Li et al., 2008; Liu et al., 2017). We show that model slab dips are also a good fit to the observed dips of the Pacific slab when the slab tail is included in the geometrical setup. In this case, the best fit model has a reduced asthenospheric viscosity of 5.1×10^{20} Pas, which results in a reduction in the excessive positive dynamic pressure build-up beneath the western Pacific Plate by a factor of approximately two thirds relative to the model of Figure 5.

6. Modeling the Global Slab System

6.1. Reference Model

Using our global plate and slab geometries and velocities (section 4), we compute the mantle pressure field that results from the motion and interactions of all plates and slabs distributed globally. Figure 6a shows an example of a model dynamic pressure field, computed for an asthenospheric viscosity of 4×10^{20} Pas, with vectors showing the vertically averaged velocity through the upper mantle (including plates). The dynamic pressure field scales linearly with viscosity so that increasing the viscosity will be reflected in a corresponding linear increase of the dynamic pressure field, while the asthenospheric velocity field will remain unchanged. We can break down the dynamic pressure field and associated asthenospheric velocities into a component due to the P_{edge} terms and a component due to the P_{wall} terms (Equations 12 and 16). Added to the asthenospheric velocities associated with the dynamic pressure field gradients is also a velocity component due to the movement of the plates (Equation 7).

The P_{edge} component of the pressure field represents the source-sink terms in the flow field. At nonslab boundaries, the P_{edge} component counterbalances the asthenospheric flow that is directly induced by the movement of the plates and provides continuity of flow across those plate boundaries. At plate boundaries with slabs, P_{wall} acts, in conjunction with P_{edge} , to set the slab-normal component of the vertically averaged velocity on both sides of the slab wall. It is these P_{wall} terms that create asymmetry and discontinuity in dynamic pressure across the slab walls. Related to this, Royden and Holt (2020) show that convergent boundaries without slabs display quasi-symmetric pressure distributions around the convergent zone; it is only the inclusion of slabs as barriers to flow that allow for asymmetric and discontinuous pressure distributions across convergent boundaries.

When the dynamic pressure field, computed for viscosity of 4×10^{20} Pas, is divided into the component due to P_{edge} functions (Figure 6b) and the component due to P_{wall} functions (Figure 6c), there is a strong hemispherical signal in the dynamic pressure associated with the P_{edge} -type functions. This pressure field is that which would be produced in the absence of slabs as barriers to upper mantle flow. It is in broad agreement with previous computations of purely plate-driven flow and the associated asthenospheric return flow (e.g., Hager & O’Connell, 1979; Schubert et al., 1978; Schubert & Turcotte, 1972; Steinberger, 2016) and reflects the large pressure gradients required to move upper mantle material away from western Pacific and Southeast Asian converging boundaries, and towards diverging boundaries, mainly in the eastern Pacific and southern Indian Ocean. The vertically averaged velocities that arise from this P_{edge} component of the pressure field generally oppose the direction of plate motion.

In contrast, the dynamic pressure associated with the P_{wall} -type functions reflects the discontinuity in dynamic pressure across the slabs. This component of the pressure field is that which arises from inserting slabs, as barriers to flow, into the mantle circulation scheme. This portion of the pressure field illustrates the strong effect that slab wall have on the pressure field around slabs, introducing a strong asymmetry into the dynamic pressure fields at subduction zones (Figure 6c). It displays a mostly regional signal in the vicinity of subduction zones, with the geographic extent of the affected region scaling approximately with length of the subduction boundary (e.g., Royden & Holt, 2020).

Figure 6d shows the RMS misfit, mean misfit, and mean difference between observed slab dip and the model slab dip computed as in the preceding section for the western Pacific slabs. These misfit metrics are

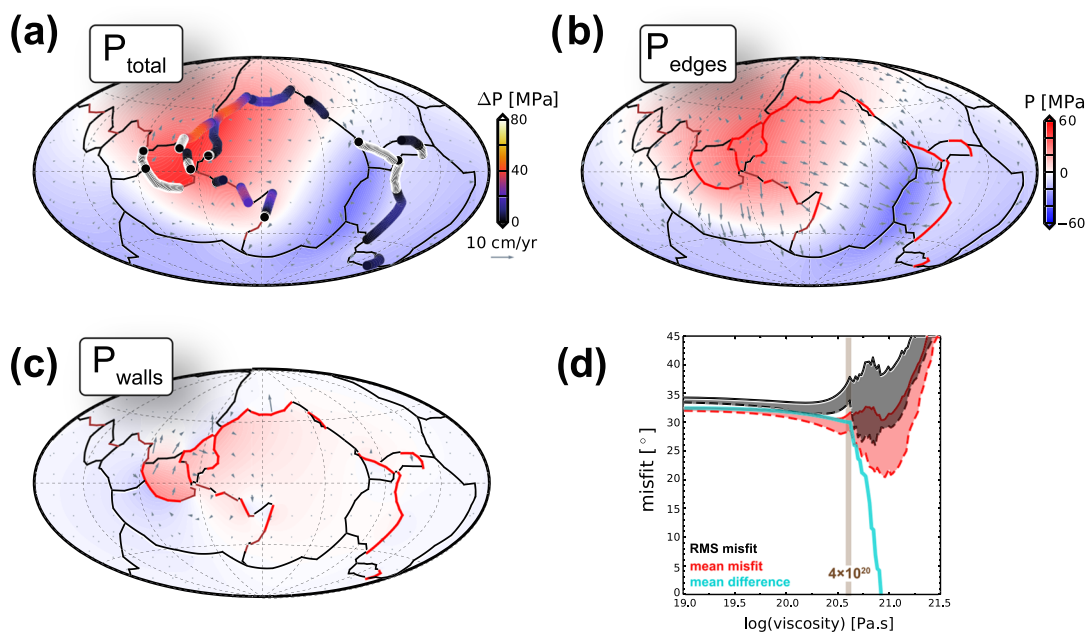


Figure 6. Computed upper mantle pressure (330 km-depth) and average asthenospheric velocity for reference, global plate geometry model with an asthenosphere viscosity of 4.0×10^{20} Pas. Panels show (a) the total dynamic pressure field, $P_{\text{total}} (= P_{\text{edge}} + P_{\text{wall}})$, (b) the P_{edge} component of dynamic pressure, and (c) the P_{wall} component of dynamic pressure. Overlaid on (a) is the total vertically averaged upper mantle velocity field (i.e., including the plates), on (b) is the P_{edge} component of the vertically averaged asthenospheric velocity (i.e., the component determined by the gradients of the P_{edge} functions), and on (c) the P_{wall} component of the vertically averaged asthenospheric velocity (i.e., the component determined by the gradients of the P_{wall} functions). Panel (a) also contains the computed differences in dynamic pressure across the slabs, ΔP , with negative values (which correspond to slab dip $> 90^\circ$) outlined in white. Panel (d) shows the global dip misfit for this model as a function of asthenospheric viscosity. Misfits plotted are the RMS misfit, the mean misfit, and the mean difference (modeled dip minus observed dip). For the RMS and mean misfits, both the misfit corresponding to when all 100-km long subduction segments are considered individually (solid lines), and the misfit when dip values are averaged over entire subduction zones, or major portions of long subduction zones (dashed lines), is shown.

computed for each individual dip angle segment in Figure 1a (solid lines) and for dip averages over each of the larger subduction zone sections labeled in Figure 1a (dashed lines). The RMS misfit is somewhat lower when dips are averaged over subduction zone segments but is still greater than $\sim 25^\circ$ for all choices of viscosity.

There is little variation in RMS misfit for asthenospheric viscosities less than $\sim 10^{20}$ Pas, with a near-constant RMS misfit of $30\text{--}35^\circ$ (Figure 6d). This reflects model slab dips that are near 90° for all slabs and results from the small magnitudes of dynamic pressure and ΔP across all slabs. For asthenospheric viscosities greater than $\sim 10^{20}$ Pas, the increasing magnitude of dynamic pressure results in model slab dips that differ significantly from 90° , but, as asthenospheric viscosity increases, the result is larger RMS misfit between observed and model slab dip for individual segments (solid black line), and only modest improvement in the RMS misfit for the larger subduction zone sections (dashed black line). For asthenospheric values much greater than 4×10^{20} Pas, RMS misfits begin to be very large due to the strong divergence of some model dips from observations (most notably at the Java/Sunda subduction zone).

Because there is no well-defined RMS minimum for the individual slab segments, we choose to display the pressure field (Figures 6a-6c) and compare model dips to observations (Figure 7) for an illustrative asthenospheric viscosity of 4×10^{20} Pas. We will refer to the results for this somewhat arbitrarily chosen value of asthenospheric viscosity as the “reference model.” Results for the reference model illustrate some of the difficulties in reconciling observed and model slab dips. Figure 7 shows the correspondence between observed and modeled dips, and “observed” and modeled dynamic pressure difference (ΔP), for the reference model. (The observed ΔP is calculated using observed dips and oceanic plate ages as described in section 4.1.3, Equation 18.) Results are shown for each dip segment (small symbols) and for averages over each major subduction boundary (large symbols).

Excluding Java/Sunda and Ryukyu, comparison of modeled and observed ΔP across the slabs shows a highly defined trend that suggests our general approach has merit. However, the slope formed by the points in

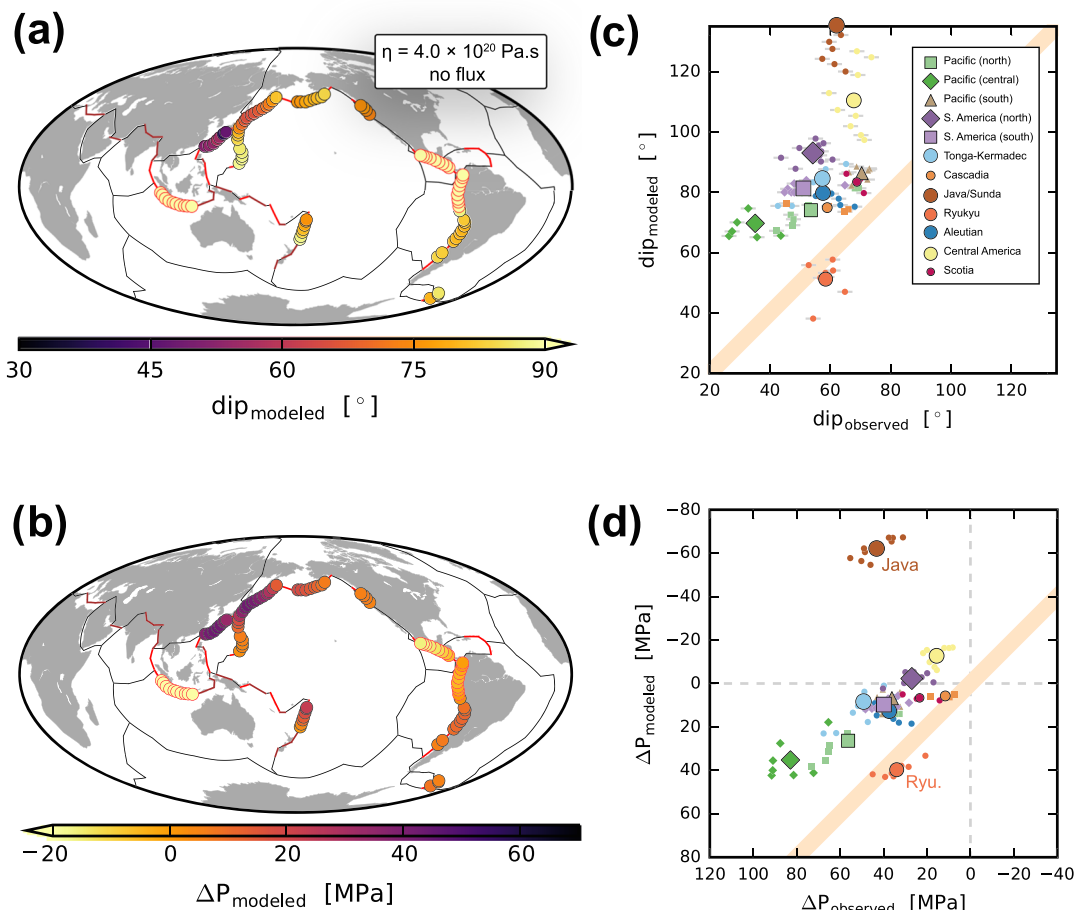


Figure 7. Comparison between observed and modeled slab dips for all major subduction zones. The model contains all of the major plates and subducting slabs and has a mantle viscosity of 4.0×10^{20} Pas. Panels show (a) map view of model dips, (b) map view of model dynamic pressure differences across slabs (ΔP), (c) scatter plot comparison of modeled and observed dips (some values for individual Java segments plot off—above—the graph), and (d) scatter plot comparison of modeled and “observed” ΔP values (Equation 18 and section 4.1.2). Larger symbols in panels (c) and (d) show dips averaged over major subduction zones or major portions of long subduction zones. Pacific slab dips are averaged over three sections divided at latitudes 32°N and 44°N, and South American subduction sections are divided at latitude 17°S.

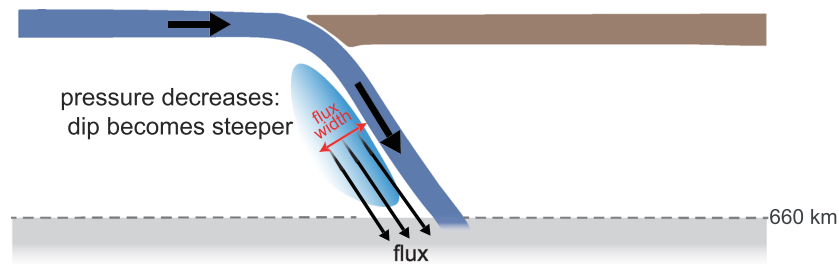
Figure 7d is approximately half that which would correspond to a perfect fit. There is also a significant offset in the trend lines, as the model values of ΔP underestimate the observed values by approximately 20–40 MPa for this asthenospheric viscosity, and Java/Sunda and Ryukyu fall particularly far from the dominant trend. Except for Ryukyu, the model dips are therefore always much steeper than the observed dips (Equation 18), with a global RMS misfit $> 30^\circ$ (Figure 6d).

Even when the Java/Sunda and Ryukyu systems—the most obvious outliers (Figures 7c and 7d)—are eliminated from computation of best fit (but included in the global flow model), the fit between model and observations is only partially improved (Figure S6). This is because of the Central America and northern South America slabs, which have positive values of the “observed” ΔP but significantly (Central America) or slightly (northern South America) negative values of model ΔP . Therefore, increasing the viscosity increases the misfit for these subduction systems. As for Java/Sunda, which has an extremely negative ΔP of -60 MPa (Figure 7d), increasing the viscosity further increases the discrepancy in ΔP at these two subduction zones, which strongly degrades the global misfit computed using individual segments (Figure 6d).

6.2. Models With Asthenospheric Flux Into the Lower Mantle

Failure to match the globally distributed slab dips in section 6.1 indicates that an important component of the global pressure field has not been modeled. The greatest source of uncertainty in this computation is

(a) subducting plate-side flux



(b) overriding plate-side flux

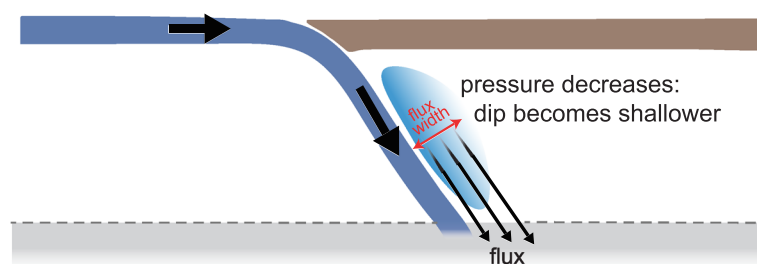


Figure 8. Illustration of the effect of upper-to-lower mantle mass flux on the mantle pressure distribution around subducting slabs. Blue regions indicate generalized location of asthenosphere fluxing into the lower mantle, parameterized as the product of a flux width (red line with arrows) and a rate of down flux. Note the across-slab pressure difference (ΔP) is only affected by the difference in down flux across the slabs (i.e., not the absolute flux amount on either side).

the nature of the lower boundary condition for the asthenosphere and the possible interchange of material between upper and lower mantle. Because the global misfit between observed and model slab dip is not remedied by changing assumptions about the nature of an impermeable basal boundary (section 6.4), we explore the effect that exchange of material between the upper and lower mantle may have on asthenospheric pressure and, in turn, slab dip.

There are multiple sites at which significant amounts of material may flow between the upper and lower mantle and thereby modify the dynamic pressure field relative to that associated with flow confined to the upper mantle. For example, significant upward flux into the upper mantle is likely to be associated with mantle plumes (e.g., Phipps Morgan et al., 1995; Yamamoto et al., 2007). Here, we consider the effects of focused downward transfer of material from upper to lower mantle at subduction zones. Figure 8 shows two possibilities for flow, or “down-flux,” of asthenosphere into the lower mantle in association with subduction, which can involve asthenosphere located above (upper plate side) or below (subducting plate side) the slab or on both sides. Down flux is implemented in our model by changing the velocity on the side of the slab wall at which down flux occurs, which mimics the effect of transferring material into the lower mantle in a zone immediately adjacent to the slab wall (section 2.2). In order to conserve mass, an equal upward flux of material from lower to upper mantle must occur somewhere. In our analytical models, we assign this upward flux to be uniformly distributed over the base of the upper mantle so that there are no lateral pressure gradients directly associated with the distributed fluxing process.

On the side of the slab where down flux of asthenosphere occurs, the dynamic pressure adjacent to the slab reduces/becomes more negative (Royden & Holt, 2020: Figures 12 and 13). This is because the pressure gradient in the asthenosphere depends on the vertically averaged velocity of the asthenosphere: increasing the average velocity in a particular direction will be associated with a change in the pressure gradient such that the gradient becomes more negative in the direction of flow. Therefore down flux into the lower mantle on the overriding plate side of a slab reduces the dynamic pressure on the overriding plate side of the slab and

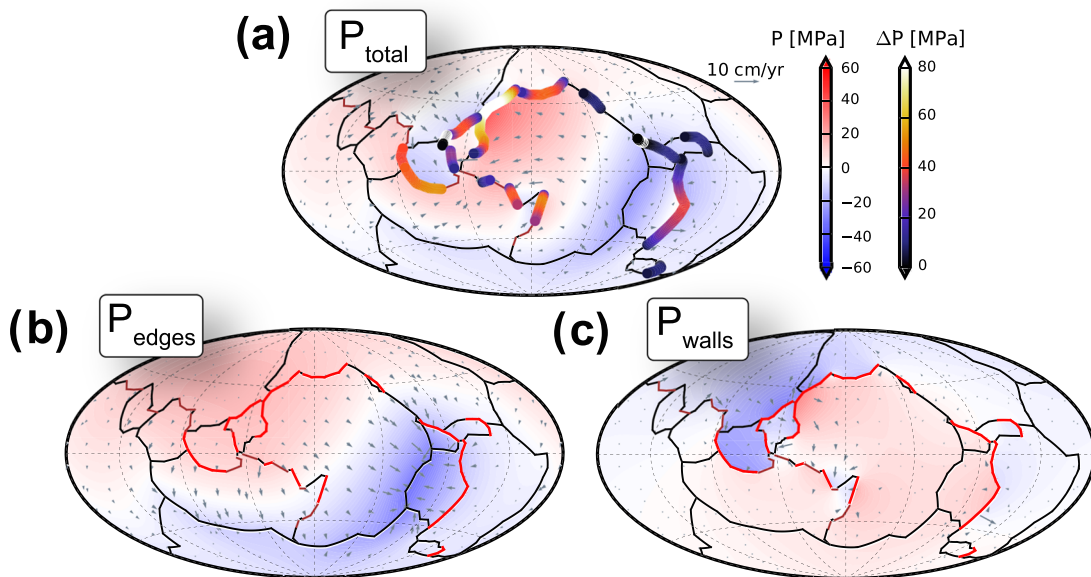


Figure 9. Computed upper mantle pressure (330-km depth) and average asthenospheric velocity for mantle down-flux flux model (mantle viscosity of 4.0×10^{20} Pas, flux width of 500 km). Panels show (a) the total dynamic pressure field, $P_{\text{total}} (=P_{\text{edge}} + P_{\text{wall}})$, (b) the P_{edge} component of dynamic pressure, and (c) the P_{wall} component of dynamic pressure. Overlain on (a) is the vertically averaged upper mantle velocity field, including the plates, on (b) is the P_{edge} component of the vertically averaged asthenospheric velocity (i.e., the component determined by the gradients of the P_{edge} functions), and (c) is the P_{wall} component of the vertically averaged asthenospheric velocity (i.e., the component determined by the gradients of the P_{wall} functions). Panel (a) also contains the computed differences in dynamic pressure across the slabs, ΔP , with negative values (which correspond to slab dip $> 90^\circ$) outlined in white.

will be reflected in shallower slab dip (Figure 8b). Conversely, down flux on the subducting plate side of the slab results in a steeper slab dip (Figure 8a).

The resulting pressure and velocity fields are sensitive only to the total flux of material, per unit length of trench, into the lower mantle and to which side of the slab the down flux occurs on. We parameterize this flux as the product of a flux velocity and a flux width. For simplicity, we take the flux velocity to be equal to the convergence velocity at each individual subduction zone segment and experiment with a variety of flux widths. Note, however, that results depend only on the product of flux velocity and flux width and so cannot be distinguished from, for example, material with twice the flux width moving into the lower mantle at half the convergence rate. In addition, it is the difference in down flux on either side of the slab that dictates the across-slab pressure difference (ΔP) in our model. While we explore models that contain down flux only on one side of the slab, we note that the same across-slab pressure differences could be obtained with down flux on both sides of the slab, provided that the difference in down flux on either side of the slab is maintained. The addition of this down-flux component is the only change made to the reference setup in section 6.1.

We ran 41 models with various flux widths (0 to 1,000 km, at 50-km intervals, on both sides of the slabs) and, for each model, examine the misfit between modeled and observed dips for a range of asthenospheric viscosities. In comparison to the reference case, with no down flux of asthenosphere, the fit between modeled and observed dips is not improved by down flux on the subducting plate side of the slab but can be significantly improved by down flux of asthenosphere on the overriding side of the slab.

We find that the lowest RMS misfit between observed and model dips occurs at a flux width of 500 km, on the overriding plate side of slab, and an asthenospheric viscosity of 4.0×10^{20} Pas (Figures 9–11). Computed over all individual segments (Figure 1a), this best fit model yields a mean misfit of 8.2° and an RMS misfit of 10.2° . If we average dips over the major subduction zones (i.e., labels in Figure 1a), the misfits reduce to a mean of 6.9° and an RMS of 8.1° . For dips averaged over subduction zones, Figure 11a shows the RMS misfit for each of the 41 flux widths and for asthenospheric viscosities that span three orders of magnitude. By combining RMS misfit with a Pearson coefficient, which measures the strength of the linear correlation between

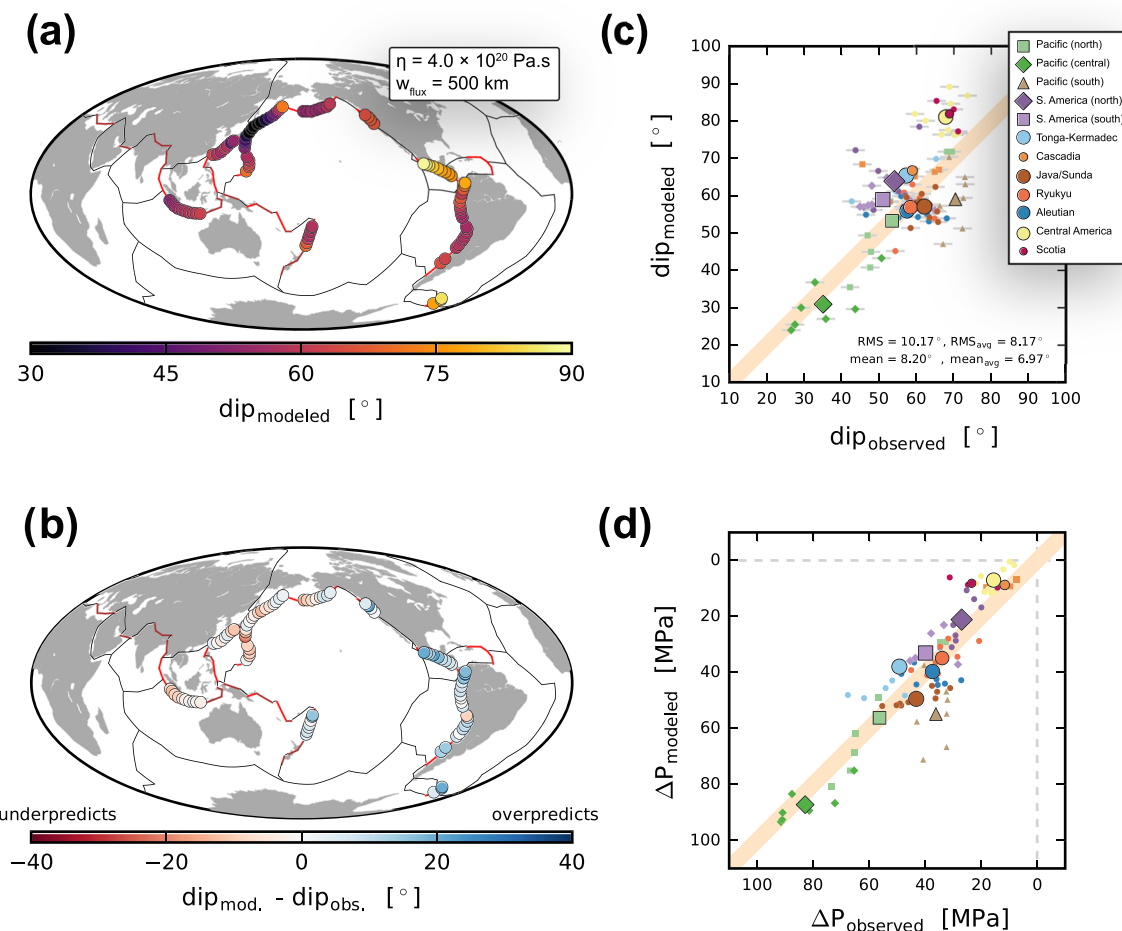


Figure 10. Comparison between observed and modeled slab dips for global model with upper mantle down flux on the overriding plate side of the slab (as displayed in Figure 9: 500-km flux width, 4.0×10^{20} -Pas viscosity). Panels show (a) map view of model dips, (b) map view of the difference in model and observed dips (ΔP), (c) scatter plot comparison of modeled and observed dips, and (d) scatter plot comparison of modeled and “observed” ΔP values (Equation 18 and section 4.1.2). Larger symbols in (b, d) show dips averaged over major subduction zones or major portions of long subduction zones.

observed and modeled dips, we define as acceptable fits those models with RMS misfit less than 15° and R_{Pearson} greater than 0.7. By this metric, we produce acceptable fits to global slab dips for flux widths on the overriding plate side of the slabs that are between 300 and 600 km and mantle viscosities between 2 and 5.6×10^{20} Pas. There are no acceptable fits between observed and model slab dips for asthenospheric viscosities outside the range of 10^{20} to 10^{21} Pas.

Our model dips for the western and northern Pacific rim correspond well with observations, with minimum slab dips of $\sim 30^\circ$ along the central part of the Pacific slab (Japan), increasing southward to $60\text{--}70^\circ$ (Marianas), continuing through the Tonga-Kermadec region at $\sim 60^\circ$ (Figure 10). From Japan northwards, the dips increase to 55° (Kamchatka) and then continue eastwards at $\sim 60^\circ$ (Aleutians). In the eastern Pacific, we retrieve the large-scale trend of slab dip in South and Central America, with slab dips increasing northward from southern South America, by $\sim 5^\circ$ in northern South America and by another $\sim 20^\circ$ in Central America (although model dips are 5–10° steeper than observed). In our models, the dip trends in both of these major subduction systems—South America and the Western Pacific—are largely dictated by along-strike variations in mantle pressure rather than by significant variation in slab buoyancy (Equation 18). Both the southward decrease in slab dip in South America and the northward and southward decrease in slab dip towards Japan in the western Pacific are a result of increased ΔP magnitudes (Figure 8a). This is clear because, as shown in Figure S7, slab age either exhibits little variability (western Pacific) or varies in the wrong direction to explain changes in slab dip as a product of changes in slab buoyancy (South

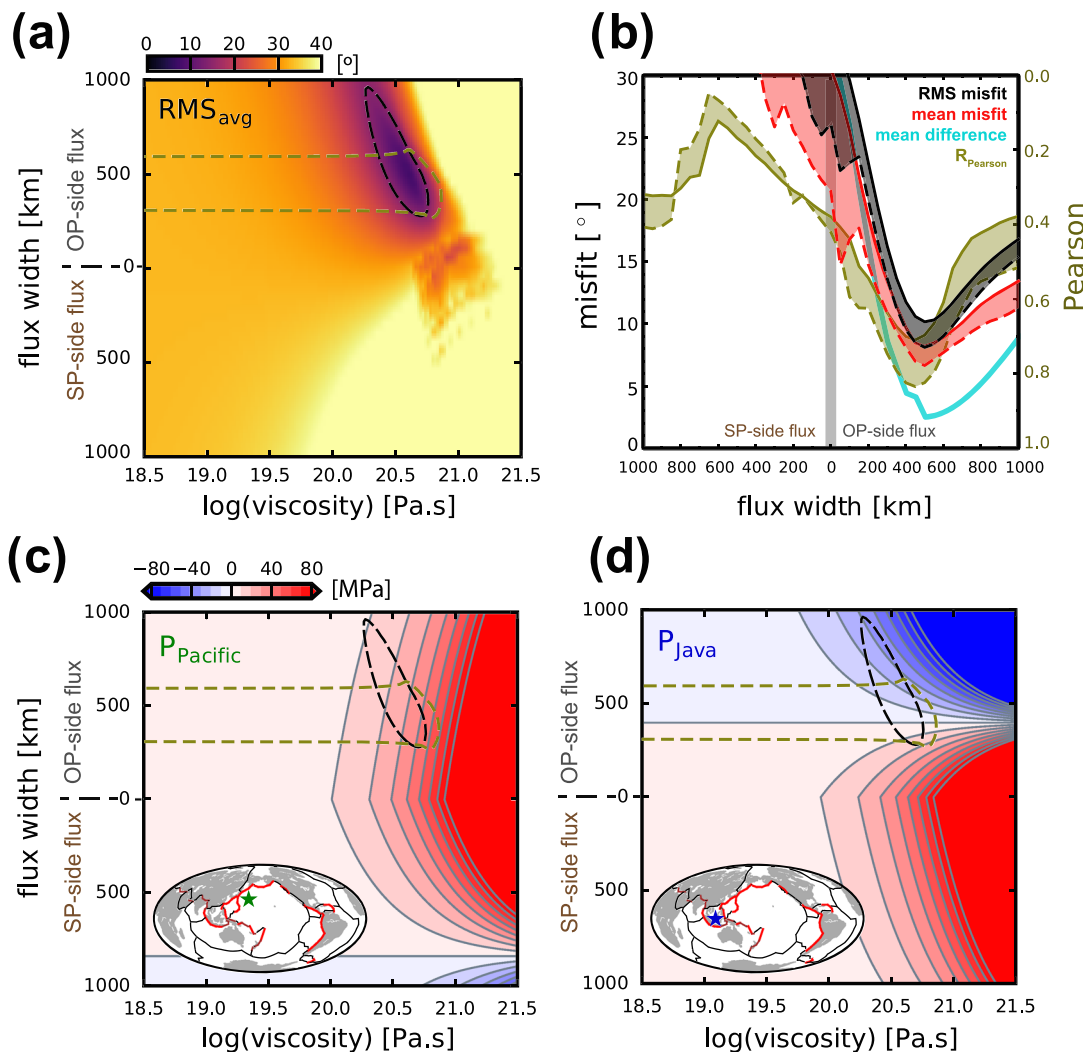


Figure 11. Global dip misfit as a function of down-flux width and asthenospheric viscosity. (a) Global RMS misfit computed using dips averaged over either entire subduction zones or large sections of big subduction zones. Dashed black line is RMS misfit = 15°; dashed gold line is Pearson's correlation coefficient = 0.7. (b) RMS misfit, mean misfit, mean difference (modeled dip minus observed dip), and Pearson's correlation coefficient as a function of down-flux width. For each metric (aside from the mean difference), and each flux width, we search for the best fit viscosity and plot the misfit values associated with this. For the mean difference, we plot the value associated with the model that gives the lowest RMS misfit (for individual segments). Solid lines correspond to the misfit when all 100-km long subduction segments are considered individually (solid lines) and dashed lines correspond to the misfit when dip values are averaged over major subduction zones or major portions of long subduction zones. Lower panels show dynamic pressure (330-km depth) as a function of model viscosities and down-flux width for two locations: (c) the western Pacific (longitude = 160°E, latitude = 30°N) and (d) Indonesia (i.e., the Java upper plate: longitude = 113°E, latitude = 3°S).

America). This points to mantle pressure as the main control on slab dip in both of these large subduction systems.

Model dips for the short Scotia subduction zone are also in reasonable agreement with observed dips but 10–15° steeper than those observed. The overprediction of slab dip (i.e., underprediction of ΔP) for the Scotia and Central American slabs is likely due to the short trench lengths in these systems. Royden and Holt (2020) demonstrate that, for short subduction zones, careful treatment of the finite-width slab region becomes important, whereas it is relatively unimportant for long slabs and large plates and so has been neglected in this global analysis.

6.3. Implications for Global Flow and Dynamic Pressure in the Asthenosphere

As before, we break down the dynamic pressures and associated asthenospheric velocities into a component due to the P_{edge} terms and a component due to the P_{wall} terms (Equations 12 and 16), recalling that the P_{edge}

component of the pressure field represents the source-sink terms in the flow field and defines the pressure field that would exist without the presence of slabs as barriers to asthenospheric flow. In both the reference case and best fit case with asthenospheric down flux, the P_{edge} component of dynamic pressure has a hemispheric distribution. In the reference case with no down flux, P_{edge} is highly positive (30–40 MPa) beneath the western Pacific and Southeast Asian subduction zones (Figure 6b). This is because large pressure gradients are needed to drive the return flow in the asthenosphere from these regions of plate convergence to regions of dominantly plate divergence, which produces a high amplitude, hemispheric pressure pattern (e.g., Hager & O'Connell, 1979; Steinberger, 2016). The P_{edge} component of the pressure field in the best fit model with asthenospheric down flux is significantly reduced with, for example, a northwestern Pacific magnitude of 10–15 MPa (cf. Figures 6b and 9b). This occurs because the transfer of asthenosphere into the lower mantle near the Pacific, Philippine Sea, and Java subduction systems reduces the volume of asthenosphere that must be fluxed laterally away from this region in the upper mantle, as shown by the reduction of the asthenospheric return flow associated with P_{edge} . Hence, the pressure gradients needed to drive the return flow, and the overall magnitude of the pressure field, are strongly reduced.

As in the reference case, the asthenospheric velocities that result from the P_{wall} component of the pressure field represent the effect of inserting slabs as barriers to upper mantle flow. As discussed in section 6.2, the P_{wall} component introduces an asymmetric pressure signal about subducting slabs that is highly sensitive to which side of the slab asthenospheric down fluxing occurs, and asthenospheric down flux reduces the dynamic pressure on the side of the slab on which it occurs (Figure 8). It is important to note that, without slabs as barriers to mantle flow, down fluxing of asthenosphere produces a quasi-symmetric reduction in dynamic pressure around the subduction zone, as is reflected in the dynamic pressures produced by the P_{edge} solutions. Without down flux on the overriding plate sides of slabs, the P_{wall} component produces pressure differences across the slabs that are, in general, 20–40 MPa less than those inferred from the observed slab dips and nearly 100 MPa less for the Java slab (Figures 6c and 7d). Only models with asthenospheric down fluxing on the overriding plate side of the slabs are therefore able to provide acceptable fits to the observed slab dips and inferred ΔP values (Figures 9 and 10).

When the P_{edge} component of the pressure field (smooth, hemispherically distributed) is combined with the P_{wall} component (regionally variable, discontinuous at slab boundaries), the combined field yields dynamic pressures of 15 to 45 MPa in the western Pacific for models that satisfy observed dips (Figure 11c) and a dynamic pressure of ~30 MPa for the best fit according to the RMS misfit computed over individual segments (Figure 9a). This contrasts with the larger, ~50-MPa pressures generated when no asthenospheric down flux occurs (Figure 6a). Assuming dynamic pressure is supported by deflections of Earth's surface (e.g., Zhong & Gurnis, 1994), this ~50 MPa would correspond to a very large water-loaded dynamic topography of positive ~2 km, while the best fit model pressures (Figure 9a), and the acceptable range (Figure 11c), correspond to a positive dynamic topography of 1.3 ± 0.7 km. Overall, the best fit model displays an increase in dynamic pressure of ~50 MPa across the Pacific Plate, from east to west (Figure 9a), although the value of this pressure increase varies substantially within the range of models that satisfy dips (Figure 11c).

6.4. Testing Models With Additional Slab Geometries and Model Parameters

In addition to the reference geometry, we have also examined the effects of alternative slab geometries in regions where the geometry or continuity of slabs is unclear. The plate geometries are well constrained and remain unchanged. We examine the effects of two geometries where shallowly subducting slabs have been removed ("no Philippine slab," and "no Papua New Guinea slab") and four cases where slab walls have been added to connect subduction systems where previously we had had a gap between slabs ("closed Aleutian," "closed Myanmar," "closed Philippine," and "closed Nankai" cases). These geometries are shown in Figure S2.

The first-order features of the model pressure fields, and model slab dips, are unchanged except in the "closed Aleutian" geometry. For the other six alternative geometries, the best global RMS misfit to the slab dip is between 9.4° and 11.4° for individual segments and between 7.2° and 9.4° when dips are averaged over subduction zones (Figure 12). The associated mantle viscosities range between 2.5×10^{20} and 4.0×10^{20} Pas and the flux widths between 450 and 550 km, although the dips can be fit reasonably well (RMS $< 15^\circ$) for flux widths greater than or equal to 350 km. Overall, the best fit between observed and modeled dips occurs

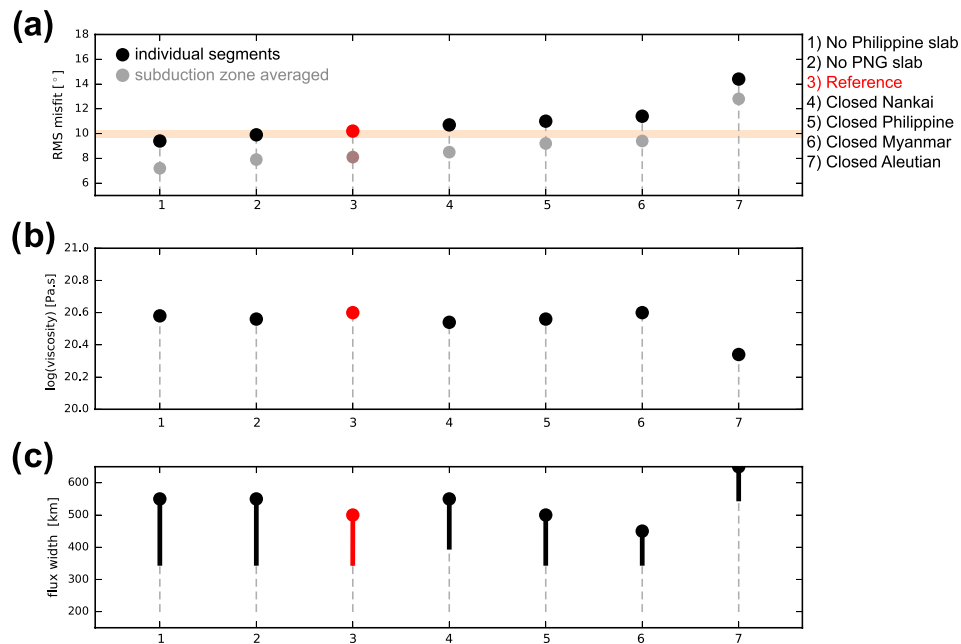


Figure 12. Comparison of models with a range of slab wall geometries. Panel (a) shows the best global dip RMS misfit (black/red), attained after searching through the flux width and mantle viscosity parameter space. For the same flux width and mantle viscosity, we also show, in gray/pink, the RMS misfit value corresponding to when dips are averaged over either entire subduction zones or large sections of big subduction zones (i.e., S. America and W. Pacific). Panels (b) and (c) show the mantle viscosity and flux width (overriding plate side) that the best fits correspond to. The bars on panel (c) extend down to the lowest flux width required for a good global dip match ($\text{RMS} < 15^\circ$).

when the shallow Philippine slab is omitted (RMS segment misfit = 9.4° , RMS averaged misfit = 7.2° ; Figure S8). Relative to the reference geometry, the primary change is a slight increase in the modeled average dip of the Japan slab (from 30° to the observed 35°).

In the “closed Aleutian” geometry, which is the only alternative slab model that significantly degrades the dip fit, the slab gap between the Kamchatka and Aleutian subduction systems is removed (Figure S2). Closing the gap blocks the available pathway for asthenospheric material to migrate from beneath the northwest Pacific Plate to beneath Eurasia, which gives rise to dynamic pressures beneath the northwestern Pacific that are $\sim 50\%$ greater than in the reference geometry. This decreases the dip of the western Pacific slabs below those observed. Relative to the reference geometry, this geometry yields an increased individual segment RMS segment misfit of 14.4° . Slab dips therefore suggest the presence of a pressure outlet in the NW Pacific, which is consistent with both an apparent lack of seismicity deeper than ~ 100 km and tomographic images that appear to show a slab gap (Lees et al., 2007; Levin et al., 2005).

We have also tested suites of additional model geometries and parameterizations, particularly models with different down flux and basal boundary parameterizations. In terms of down flux, these include models within which the upper to lower mantle flux velocity is set at a constant 5 cm/year for all slabs rather than varying linearly with local convergence rate (Figures S9 and S10) and models within which down flux is constrained to only occur at certain subduction boundaries (Figure S11). In terms of basal boundary conditions, we additionally examine models that include the Japan “slab tail”—the portion of the subducting Pacific Plate that lies flat atop the lower mantle beneath Japan and adjacent parts of Eurasia (Figures S12 and S13)—and models with a no-slip lower boundary (Figures S14 and S15).

Imposing a constant down flux velocity does not change the primary features of the model pressure field, and these models provide a reasonable fit to the observed slab dips, with a slightly increased individual segment RMS misfit (10.9–12.1° except for the closed Aleutian case, where it was larger). Limiting down flux to the Java subduction zone, the Western Pacific subduction zones, or both did not provide a good fit between observed and model slab dips (Figure S11) and did not significantly improve the fit relative to the no down-flux reference case of section 6.1 (RMS misfit $\geq 20^\circ$). Constraining down flux to occur only at slabs

that appear to penetrate into the lower mantle (e.g., Van der Meer et al., 2018) produces a broadly acceptable fit to slab dips but increases the RMS misfit by 3–4° relative to the reference case with down flux at all slabs (Figure S11e). The combined results of these alternative models suggest that down flux of asthenosphere into the lower mantle occurs at subduction zones globally and may, but does not necessarily, scale with the rate of subduction along individual subduction systems.

Testing the role of the Pacific slab tail beneath Japan requires a reduction in the thickness of the asthenosphere in this region, and the choice of a free-slip or fixed velocity ($=V_{\text{Pacific}}$) mechanical boundary condition at the top of the flat-lying tail (e.g., Figure 2). Assuming the slab tail thickness is equivalent that of the surface plates (80 km), the asthenospheric thickness a locally reduces to 500 km. A free-slip Pacific slab tail does not significantly change the model pressure field and slightly improves the RMS dip misfit by about a degree (Figures S12 and S13). A fixed velocity Japan slab tail greatly reduces the asthenospheric pressure above the slab tail and produces model slab dips for Ryukyu and central Pacific slabs that are much shallower than the observed dips for all slab geometries that, in turn, degrades the best dip misfit to RMS > 14° (Figures S12). This result suggests that if the Pacific slab tail is moving rapidly westward along the base of the upper mantle, it is either mechanically decoupled from the overlying mantle (or equivalently, the asthenospheric viscosity above the slab tail is anomalously low).

Unlike in free-slip base models, the reference frame of the imposed plate and slab velocities strongly affects the results in the case of a no-slip basal boundary condition. When a no net rotation reference frame is adopted for the plate and slab velocities, we find that the best fit model pressure fields, and hence the misfit between observed and model slab dips, are similar to the free-slip reference (Figure S14; best individual segment RMS misfit = 9.5°). However, as expected when a fixed velocity base is imposed, the asthenospheric viscosities for the best fit result are reduced by about a factor of 4 to $\approx 10^{20}$ Pas (Royden & Holt, 2020). In contrast, when a hotspot reference frame is adopted (HS3; Gripp & Gordon, 2002), the misfit increases significantly to 16.4° (Figure S15). This is due to elevated positive pressure build-up beneath Sundaland that, in this reference frame, occurs even when significant down flux is imposed on the overriding plate side of the slab.

7. Model Limitations

Our analytical method adopts a number of physical simplifications that facilitate extraction of the governing, first-order physics and enable calculations that are not computationally demanding. In so doing, we are able to explicitly incorporate subducting slabs as barriers to flow in the asthenosphere but neglect the role that nonslab density and viscosity variations play in dictating mantle pressure patterns. For example, vertical variations in mantle viscosity associated with a thin and weak layer beneath the lithosphere are likely to modify upper mantle flow and pressure fields relative to that of our isoviscous upper mantle models (e.g., Becker, 2017; Hoink & Lenardic, 2010; Lenardic et al., 2019). Vertical viscosity variations can be incorporated via the “viscosity coefficient” prefactor of our pressure solutions. As discussed in section 8, and more quantitatively in our companion paper (Royden & Holt, 2020: section 5.2), a weaker, shallower upper mantle layer is expected to produce a pressure field that is more sensitive to the lateral motions of the vertical slab walls relative to those of the surface plates. Similarly, lateral variations in the effective viscosity of the asthenosphere, as associated with thermal anomalies or non-Newtonian flow (i.e., dislocation creep), have been shown to affect subduction dynamics and slab dips (e.g., Billen & Hirth, 2005, 2007; Holt & Becker, 2016) and so could also potentially modify the across-slab pressure differences associated with our isoviscous upper mantle models. In our method, lateral viscosity variations can be approximated by dividing plates up into smaller domains (each with the same plate velocities but different sublithospheric viscosity structures), but this is beyond the scope of the current study.

Another simplification made in this paper is that circulation is confined to the upper mantle except (i) down flux adjacent to subduction zones and (ii) a compensating flux from lower to upper mantle that is uniformly distributed over the base of the upper mantle. We therefore neglect any active role that the lower mantle may play in organizing upper mantle flow and the associated dynamic pressure in the upper mantle. In the supporting information of Holt et al. (2018), we show that overall subduction-induced patterns of dynamic pressure in regional subduction models do not change substantially with the incorporation of a viscous lower mantle. Despite this, the amplitude of the pressure field is significantly reduced (e.g., Pusok &

Stegman, 2019), which could be counterbalanced, in our approach, by a decrease in the assumed viscosity of the upper mantle.

In regions where large-scale flow cells may be developed in the lower mantle—e.g., return flow cells in response to slab penetration into the lower mantle (e.g., Faccenna et al., 2013, 2017; Husson et al., 2012)—these cells may connect regions of large-scale upwelling and downwelling and accordingly affect the mantle pressure distribution (e.g., Becker & Faccenna, 2011). However, unless these regional-scale cells translate material from one side of the slab to the other, it seems unlikely that they will have a significant effect on the pressure discontinuity across slabs in the upper mantle. More problematic are global circulation patterns that might occur in the lower mantle and are driven by lower mantle buoyancy sources (e.g., Lithgow-Bertelloni & Richards, 1998). The implications of such lower mantle circulation patterns for our slab dip results are unclear, but significant effects could result from large volume flux into the upper mantle, with focused upward fluxing on scales comparable to the total volume flux of slab material into the lower mantle.

8. Discussion

We have developed a method to directly include subducting slabs within an instantaneous, analytical computation of upper mantle flow in order to investigate links between deep slab dips and large-scale mantle flow. We parameterize subducting slabs as vertical barriers to mantle flow that penetrate and move laterally through the upper mantle. This analytical parameterization has been successfully benchmarked against regional, 3-D numerical subduction models (Royden & Holt, 2020), which demonstrate the ability of our analytical method to capture the first-order features of the flow and dynamic pressure fields associated with subduction zones.

By relating slab dip to slab buoyancy and the difference in dynamic pressure across the slab (ΔP , Equation 18), we predict slab dips using our modeled pressure fields. We are able to fit some regional patterns of slab dip, most notably in the western Pacific, using only regional constraints on mantle circulation (i.e., a model that includes only the Pacific and Philippine Sea plates). Here, the Pacific slab exhibits a strong along-strike variation in dip, between $\sim 30^\circ$ and $> 70^\circ$. This slab is old and highly negatively buoyant everywhere, indicating that these variations in slab dip are not due to flexural support. The good fit between observed and model slab dip therefore demonstrates that slab dip is not only dictated by slab buoyancy but also by the pressure difference (ΔP) across the slab, which here reflects the geometry of the Pacific plate and its western subduction boundary (e.g., Holt et al., 2018).

Although slab dip in the western Pacific can be explained with a model that contains only the Pacific and Philippine Sea plates (e.g., Figure 5), it is likely that the success of this “regional” model is due to the large size and rapid velocity of the Pacific plate, which dominates the global pressure field. For most other slabs, our work shows that matching the deep slab dip requires flow in the asthenosphere on a global scale. This result builds on those of Hager and O’Connell (1978) and Husson (2012) who make convincing cases for the global pattern of slab dip and trench motion, respectively, being best reconciled in a global mantle flow context. It is also consistent with studies that show that there is not a strong correlation between deep slab dip and most regional subduction-related parameters (such as slab age and subduction velocity; e.g., Jarrard, 1986; Cruciani et al., 2005; Heuret & Lallemand, 2005; Lallemand et al., 2005).

Our work indicates that the global distribution of slab dips can be used to constrain upper mantle processes on a global scale, via the dependence of slab dip on dynamic pressure (through ΔP). Because deep slab dips on Earth are less than 90° , the dynamic pressure on the overriding plate side of subducting slabs must be less (i.e., more negative) than the dynamic pressure beneath the slab. The requisite difference in dynamic pressure across a slab may be produced by positive dynamic pressure beneath the slab (notably beneath the central western Pacific slab, with 30 ± 15 MPa below the slab, Figure 11c) and/or by negative dynamic pressure above the slab (for example, Java/Sunda, with -10 ± 20 MPa above the slab, Figure 11d).

While this sense of dynamic pressurization agrees with the local pressure pattern associated with mantle wedge corner flow (e.g., Stevenson & Turner, 1977; Tovish et al., 1978), this effect of corner flow is only significant in the very shallow asthenosphere. Analytical computations show that by 200–300-km depth, the dynamic pressure associated with wedge flow is negligible compared to the dynamic pressures induced by global flow (e.g., Stevenson & Turner, 1977; Tovish et al., 1978). Deep slab dip can therefore be related

only to differences in dynamic pressure above and beneath slab that are induced by large-scale flow in the asthenosphere.

In order to produce dynamic pressures that agree satisfactorily with the global distribution of slab dips, our model increases the difference in dynamic pressure (ΔP) across all slabs by fluxing significant volumes of asthenosphere downwards into the lower mantle (e.g., Royden & Holt, 2020). Down flux of asthenosphere occurs adjacent to the slab and, surprisingly, on the overriding plate side of the slab. (An alternative mechanism is to flux material upwards, from lower to upper mantle, on the subducting plate side of the slab, but we consider this to be less geodynamically feasible.) Down flux of asthenosphere is most obviously needed at the Java/Sunda subduction zone (cf. Figures 6 and 9), but we find that restricting down flux to only Java/Sunda or the western Pacific slabs plus Java/Sunda does not produce a satisfactory match to global slab dip, with Central America and South America remaining important outliers. Therefore, it appears that the process responsible for down flux on the upper plate side of slabs, or some alternative mechanism to systematically increase ΔP magnitudes, is a global phenomenon. This incorporation of material down flux enables us to generate an upper mantle pressure field that is consistent with the global distribution of slab dips (Figure 9a).

If we were to have computed dynamic pressure using analytical models with a depth-dependent upper mantle viscosity, down flux on the upper plate side of the slabs would still be required to fit the global distribution of slab dip. However, for the case of a two-layer upper mantle, where the upper layer has a viscosity that is several times lower than the lower layer (e.g., Gutenberg, 1959; Richards et al., 2001), the magnitude of down flux needed to obtain a good fit would be reduced by an amount dependent on the viscosity contrast between the upper and lower layer (see Royden & Holt, 2020: Section 5.2). For two equally thick layers, the volume rate of down flux from upper to lower mantle, adjacent to the slabs, would be reduced by ~20% if the upper layer were a factor of 2 less viscous than the lower layer and by ~40% if the upper layer were a factor of 10 less viscous than the lower layer (Royden & Holt, 2020: Equation 36).

The cause for the large-scale down flux of asthenosphere into the lower mantle is unclear. It is possible that the inferred down flux is a proxy for some processes or properties that are not encapsulated in our model. While we examined, and ruled out, the effect of thickened lithosphere, and reduced asthenospheric thickness, beneath continental regions, it is possible that global-scale variations in mantle viscosity, or the effects of nonlinear viscosity, could create the effect on mantle pressure variation needed to explain global slab dips without this additional down flux. Various studies have also explored the possibility of entrainment of a weak, thin, and buoyant sublithospheric layer into the lower mantle at subduction zones (e.g., Phipps Morgan & Morgan, 1999; Phipps Morgan et al., 2007). While this corresponds to down flux on the subducting plate side of slabs, the wedge-directed buoyancy force associated with a low density sub-slab layer is an alternative, flux-related mechanism that could potentially produce a systematic decrease in slab dips (Liu & Zhou, 2015). Alternatively, the down flux on the overriding plate side of slabs (i.e., as is implemented in our models), which is several times that represented by the descent of slabs into the lower mantle, could potentially be a result of processes that increase the density of the upper mantle on the overriding plate side of subduction boundaries (e.g., the exothermic phase transition of olivine to wadsleyite at depths of ~410 km).

In our model, the largest variations in dynamic pressure across a single plate occurs across the Pacific Plate, where dynamic pressure increases westward, from the East Pacific Rise to the Japan slab region, by ~50 MPa. Assuming support by dynamic perturbations of Earth's free surface, these western Pacific dynamic pressures correspond to (water-loaded) positive dynamic topography of approximately 1.3 ± 0.7 km (Figure 11c). Broadly distributed dynamic topography, such as that obtained in our study, could potentially produce little geoid signal if there is a corresponding deflection of the density contrast at the base of the upper mantle (e.g., Yamamoto et al., 2007).

Such large magnitudedynamic topography in oceanic basinsis in disagreement with observational studies that suggest dynamic topography is limited to magnitudes on the order of 500 m (e.g., Hoggard et al., 2016; Watkins & Conrad, 2018), but in broad agreement with the larger amplitudes associated with some global numerical mantle flow calculations (e.g., Steinberger et al., 2019; Yang et al., 2017). However, within global numerical mantle flow calculations, such large amplitude dynamic topography signals are typically associated with large-scale flow throughout the entire mantle due to internal density anomalies, both factors

of which are absent in our slab and plate-driven models, which often results in opposing topography (/dynamic pressure) patterns (e.g., negative dynamic topography in the western Pacific, relative to positive in our analytical models). Reconciling lower amplitude, observationally based dynamic topography estimates may therefore be possible by combining the dynamic topography associated with whole mantle structure with some form of the upper mantle signal of our models that is required to satisfy slab dips. In addition, these results support previous suggestions that a component of the departure of ocean floor subsidence from that predicted by half-space cooling may have dynamic origins in the asthenosphere (e.g., Cazenave & Lago, 1991; Phipps Morgan & Smith, 1992). A cursory examination of pressure distribution in Figure 9 indicates that the dynamic topography resulting from upper mantle circulation would contribute to the shallowing of the oldest Pacific lithosphere in the western Pacific by about a kilometer, as is broadly comparable to the deviation of observed Pacific subsidence from the predictions of half-space cooling (e.g., Hillier & Watts, 2005; Zhong et al., 2007).

9. Conclusions

We have developed an analytical tool to compute upper mantle flow in a global spherical annulus based on a previous Cartesian version that is benchmarked against numerical subduction models (Royden & Holt, 2020). Within our flow computation, we incorporate subduction zones as vertical barriers to mantle flow, which enables us to probe feedbacks between subduction systems and global flow.

Slab dips can be related to dynamic pressure in the surrounding mantle via a simple force balance (e.g., Holt et al., 2017). We exploit this in order to convert our model pressure fields to slab dip predictions and compare these predictions with dips extracted from the Slab2 observational model (Hayes et al., 2018). Overall, we find that slab dips are indeed well matched in a global flow context within which the forces that mantle flow exerts on slabs are accounted for. By varying the mantle viscosity and the amount of material that fluxes into the lower mantle at subduction zones, we are able to produce global mean and RMS dip misfits as low as 7° and 9°, respectively, for individual subduction segments (and for averages over the major subduction zones, misfits as low as 6° and 7°, respectively).

These optimal fits correspond to reasonable upper mantle viscosities (2.5×10^{20} to 4.0×10^{20} Pas) and require the addition of a large material flux into the lower mantle flux on the upper plate side of the slab (downflux at rates equivalent to a width of ≥ 300 -km fluxing into the lower mantle at the local convergence velocity). Without this material flux, which decreases the dynamic pressure on the upper plate side of the slab, modeled dips angles are too steep and, in some cases (Java, Central America), overturned (dip $> 90^\circ$).

Robust features of our optimal models include negative dynamic pressure on the upper plate side of all subducting slabs and positive dynamic pressure build up beneath the western Pacific Plate (30 ± 15 MPa). In our models, the correct dip trends in both the western Pacific and South American subduction zones occur as a result of along-strike variations in mantle pressure rather than changes in slab buoyancy (Equation 18). In particular, the Western Pacific decrease in slab dip towards Japan, and the southward dip decrease in South America, are both due to increased ΔP magnitudes that are a function of large-scale mantle flow regime.

Our results substantiate previous work that suggests reconciling Earth's global pattern of slab dips requires a global, mantle flow perspective (Hager & O'Connell, 1978). Conversely, we show that slab dips offer a potential window into global mantle processes due to their dependence on dynamic pressure distribution.

Acknowledgments

We thank Clint Conrad, Boris Kaus, Fabio Crameri, and an anonymous reviewer for thoughtful reviews that significantly improved the manuscript. We also thank Clint for previous discussion about pressure and topography, which strengthened our interpretation of the modeling results. The Python code needed to run models, plot pressure fields, and analyze dips is available in the following permanent repository (<https://doi.org/10.5281/zendono.3774385>).

References

- Alisic, L., Gurnis, M., Stadler, G., Burstedde, C., & Ghosh, O. (2012). Multi-scale dynamics and rheology of mantle flow with plates. *Journal of Geophysical Research*, 117, B10402. <https://doi.org/10.1029/2012JB009234>
- Argus, D. F., Gordon, R. G., & DeMets, C. (2011). Geologically current motion of 56 plates relative to the no-net-rotation reference frame. *Geochemistry, Geophysics, Geosystems*, 12, Q11001. <https://doi.org/10.1029/2011GC003751>
- Batchelor, G. (2000). *An introduction to fluid dynamics (Cambridge Mathematical Library)*. Cambridge: Cambridge University Press. <https://doi.org/10.1017/CBO9780511800955>
- Becker, T. W. (2017). Superweak asthenosphere in light of upper mantle seismic anisotropy. *Geochemistry, Geophysics, Geosystems*, 18, 1986–2003. <https://doi.org/10.1002/2017GC006886>
- Becker, T. W., & Faccenna, C. (2011). Mantle conveyor beneath the Tethyan collisional belt. *Earth and Planetary Science Letters*, 310, 453–461.
- Becker, T. W., Faccenna, C., O'Connell, R. J., & Giardini, D. (1999). The development of slabs in the upper mantle: Insights from experimental and laboratory experiments. *Journal of Geophysical Research*, 104, 15,207–15,226.

- Becker, T. W., & O'Connell, R. J. (2001). Predicting plate velocities with mantle circulation models. *Geochemistry, Geophysics, Geosystems*, 2(12), 1060. <https://doi.org/10.1029/2001GC000171>
- Bellahsen, N., Faccenna, C., & Funiciello, F. (2005). Dynamics of subduction and plate motion in laboratory experiments: Insights into the “plate tectonics” behavior of the Earth. *Journal of Geophysical Research*, 110, B01401. <https://doi.org/10.1029/2004JB002999>
- Billen, M. I., & Hirth, G. (2005). Newtonian versus non-Newtonian upper mantle viscosity: Implications for subduction initiation. *Geophysical Research Letters*, 32, L19304. <https://doi.org/10.1029/2005GL023457>
- Billen, M. I., & Hirth, G. (2007). Rheological controls on slab dynamics. *Geochemistry, Geophysics, Geosystems*, 8. <https://doi.org/10.1029/2007GC001597>
- Capitanio, F. A., Stegman, D. R., Moresi, L., & Sharples, W. (2010). Upper plate controls on deep subduction, trench migrations and deformations at convergent margins. *Tectonophysics*, 483, 80–92.
- Cazenave, A., & Lago, B. (1991). Long wavelength topography, seafloor subsidence and flattening. *Geophysical Research Letters*, 18(7), 1257–1260. <https://doi.org/10.1029/91GL010605>
- Conrad, C. P., & Husson, L. (2009). Influence of dynamic topography on sea level and its rate of change. *Lithosphere*, 1(2), 110–120. <https://doi.org/10.1130/L132.1>
- Cramer, F., & Tackley, P. J. (2014). Spontaneous development of arcuate single-sided subduction in global 3-D mantle convection models with a free surface. *Journal of Geophysical Research: Solid Earth*, 119, 5921–5942. <https://doi.org/10.1002/2014JB010939>
- Cruciani, C., Carminati, E., & Doglioni, C. (2005). Slab dip vs. lithospheric age: No direct function. *Earth and Planetary Science Letters*, 238(3–4), 298–310. <https://doi.org/10.1016/j.epsl.2005.07.025>
- Enns, A., Becker, T. W., & Schmeling, H. (2005). The dynamics of subduction and trench migration for viscosity stratification. *Geophysical Journal International*, 160, 761–775.
- Faccenna, C., Becker, T. W., Conrad, C. P., & Husson, L. (2013). Mountain building and mantle dynamics. *Tectonics*, 32, 80–93. <https://doi.org/10.1029/2012TC003176>
- Faccenna, C., Oncken, O., Holt, A. F., & Becker, T. W. (2017). Initiation of the Andean orogeny by lower mantle subduction. *Earth and Planetary Science Letters*, 463, 189–201. <https://doi.org/10.1016/j.epsl.2017.01.041>
- Funiciello, F., Faccenna, C., Giardini, D., & Regenauer-Lieb, K. (2003). Dynamics of retreating slabs: 2. Insights from three-dimensional laboratory experiments. *Journal of Geophysical Research*, 108(B4), 2207. <https://doi.org/10.1029/2001JB000896>
- Gripp, A. E., & Gordon, R. G. (2002). Young tracks of hotspots and current plate velocities. *Geophysical Journal International*, 150, 321–361.
- Gutenberg, B. (1959). *Physics of the Earth's interior*. New York: Springer.
- Hager, B. H. (1984). Subducted slabs and the geoid: Constraints on mantle rheology and flow. *Journal of Geophysical Research*, 89, 6003–6015.
- Hager, B. H., & O'Connell, R. (1978). Subduction zone dip angles and flow driven by plate motion. *Tectonophysics*, 50(2–3), 111–133.
- Hager, B. H., & O'Connell, R. (1979). Kinematic models of large-scale flow in the Earth's mantle. *Journal of Geophysical Research*, 84(B3), 1031–1048.
- Harper, J. F. (1978). Asthenosphere flow and plate motions. *Geophysical Journal Royal of the Astronomical Society*, 55, 87–110.
- Hayes, G. P., Moore, G. L., Portner, D. E., Hearne, M., Flamme, H., Furtney, M., & Smoczyk, G. M. (2018). Slab2, a comprehensive subduction zone geometry model. *Science*, 362(6410), 58–61.
- Heuret, A., & Lallemand, S. (2005). Plate motions, slab dynamics and backarc deformation. *Physics of the Earth and Planetary Interiors*, 149, 31–51.
- Hillier, J. K., & Watts, A. B. (2005). Relationship between depth and age in the North Pacific Ocean. *Journal of Geophysical Research*, 110, B02405. <https://doi.org/10.1029/2004JB003406>
- Hoggard, M. J., White, N., & Al-Attar, D. (2016). Global dynamic topography observations reveal limited influence of large-scale mantle flow. *Nature Geoscience*, 9, 456–463. <https://doi.org/10.1038/NGEO2709>
- Hoink, T., & Lenardic, A. (2010). Long wavelength convection, Poiseuille–Couette flow in the low-viscosity asthenosphere and the strength of plate margins. *Geophysical Journal International*, 180, 23–33.
- Holt, A. F., & Becker, T. W. (2016). The effect of a power-law mantle viscosity on trench retreat rate. *Geophysical Journal International*, 208, 491–507. <https://doi.org/10.1093/gji/ggw392>
- Holt, A. F., Becker, T. W., & Buffett, B. A. (2015). Trench migration and overriding plate stress in dynamic subduction models. *Geophysical Journal International*, 201(1), 172–192. <https://doi.org/10.1093/gji/ggv011>
- Holt, A. F., Buffett, B. A., & Becker, T. W. (2015). Overriding plate thickness control on subducting plate curvature. *Geophysical Research Letters*, 42, 3802–3810. <https://doi.org/10.1002/2015GL063834>
- Holt, A. F., Royden, L. H., & Becker, T. W. (2017). The dynamics of double slab subduction. *Geophysical Journal International*, 209(1), 250–265. <https://doi.org/10.1093/gji/ggw496>
- Holt, A. F., Royden, L. H., Becker, T. W., & Faccenna, C. (2018). Slab interactions in 3-D subduction settings: The Philippine Sea Plate region. *Earth and Planetary Science Letters*, 489, 72–83. <https://doi.org/10.1016/j.epsl.2018.02.024>
- Hu, J., & Gurnis, M. (2020). Subduction duration and slab dip. *Geochemistry, Geophysics, Geosystems*, 21, e2019GC008862. <https://doi.org/10.1029/2019GC008862>
- Husson, L. (2012). Trench migration and upper plate strain over a convecting mantle. *Physics of the Earth and Planetary Interiors*, 212–213, 32–43. <https://doi.org/10.1016/j.pepi.2012.09.006>
- Husson, L., Conrad, C. P., & Faccenna, C. (2012). Plate motions, Andean orogeny, and volcanism above the South Atlantic convection cell. *Earth and Planetary Science Letters*, 317–318, 126–135.
- Jarrard, R. D. (1986). Relations among subduction parameters. *Reviews of Geophysics*, 24, 217–284.
- Lallemand, S., Heuret, A., & Boutelier, D. (2005). On the relationships between slab dip, back-arc stress, upper plate absolute motion, and crustal nature in subduction zones. *Geochemistry, Geophysics, Geosystems*, 6, Q09006. <https://doi.org/10.1029/2005GC000917>
- Lee, C.-T. A., & Chen, W.-P. (2007). Possible density segregation of subducted oceanic lithosphere along a weak serpentinite layer and implications for compositional stratification of the Earth's mantle. *Earth and Planetary Science Letters*, 253(3). <https://doi.org/10.1016/j.epsl.2006.12.022>
- Lees, J. M., Vandecar, J., Gordeev, E., Ozerov, A., Brandon, M., Park, J., & Levin, V. (2007). Three dimensional images of the Kamchatka-Pacific Plate cusp. In *Volcanism and Subduction: The Kamchatka Region*, AGU Geophysical Monograph Series (Vol. 172, pp. 65–75). Washington, D.C.: American Geophysical Union.
- Lenardic, A., Weller, M., Höink, T., & Seales, J. (2019). Toward a boot strap hypothesis of plate tectonics: Feedbacks between plates, the asthenosphere, and the wavelength of mantle convection. *Physics of the Earth and Planetary Interiors*, 296, 106,299. <https://doi.org/10.1016/j.pepi.2019.106299>

- Levin, V., Shapiro, N., Park, J., & Ritzwoller, M. (2005). Slab portal beneath the western Aleutians. *Geology*, 33(4), 253–256.
- Li, C., van der Hilst, R. D., Engdahl, R. E., & Burdick, S. (2008). A new global model for P wave speed variations in Earth's mantle. *Geochemistry, Geophysics, Geosystems*, 9, Q05018. <https://doi.org/10.1029/2007GC001806>
- Lithgow-Bertelloni, C., & Richards, M. A. (1998). The dynamics of Cenozoic and Mesozoic plate motions. *Reviews of Geophysics*, 36, 27–78.
- Liu, L., & Zhou, Q. (2015). Deep recycling of oceanic asthenosphere material during subduction. *Geophysical Research Letters*, 42, 2204–2211. <https://doi.org/10.1002/2015GL063633>
- Li, X., Zhao, D., Li, S., & Wei, W. (2017). Age of the subducting Pacific slab beneath East Asia and its geodynamic implications. *Earth and Planetary Science Letters*, 464, 166–174.
- Mallard, C., Coltice, N., Seton, M., Muller, R. D., & Tackley, P. J. (2016). Subduction controls the distribution and fragmentation of Earth's tectonic plates. *Nature*, 535, 140–143. <https://doi.org/10.1038/nature17992>
- Müller, R. D., Sdrolias, M., Gaina, C., & Roest, W. R. (2008). Age, spreading rates and spreading symmetry of the world's ocean crust. *Geochemistry, Geophysics, Geosystems*, 9, Q04006. <https://doi.org/10.1029/2007GC001743>
- Parmentier, E. M., & Oliver, J. E. (1979). A study of shallow mantle flow due to the accretion and subduction of lithospheric plates. *Geophysical Journal of the Royal Astronomical Society*, 57, 1–22.
- Phipps Morgan, J., Hasencllever, J., Hort, M., Rüpke, L., & Parmentier, E. M. (2007). On subducting slab entrainment of buoyant asthenosphere. *Terra Nova*, 19, 167–173.
- Phipps Morgan, J., & Morgan, W. J. (1999). Two-stage melting and the geochemical evolution of the mantle: A recipe for mantle plum-pudding. *Earth and Planetary Science Letters*, 170(3), 215–239.
- Phipps Morgan, J., Morgan, W. J., Zhang, Y.-S., & Smith, W. H. F. (1995). Observational hints for a plume-fed sub-oceanic asthenosphere and its role in mantle convection. *Journal of Geophysical Research*, 100, 12,753–12,768.
- Phipps Morgan, J., & Smith, W. H. F. (1992). Flattening of the seafloor depth-age curve as a response to asthenospheric flow. *Nature*, 359, 524–527.
- Piromallo, C., Becker, T. W., Funiciello, F., & Faccenna, C. (2006). Three dimensional instantaneous mantle flow induced by subduction. *Geophysical Research Letters*, 33, L08304. <https://doi.org/10.1029/2005GL025390>
- Pusok, A. E., & Stegman, D. (2019). Formation and stability of same-dip double subduction systems. *Journal of Geophysical Research: Solid Earth*, 125, 7387–7412. <https://doi.org/10.1029/2018JB017027>
- Ribe, N. M. (2010). Bending mechanics and mode selection in free subduction: A thin-sheet analysis. *Geophysical Journal International*, 180, 559–576.
- Ricard, Y., & Vigny, C. (1989). Mantle dynamics with induced plate tectonics. *Journal of Geophysical Research*, 94, 17,543–17,559.
- Richards, M. A., Yang, W., Baumgardner, J. R., & Bunge, H. (2001). Role of a low-viscosity zone in stabilizing plate tectonics: Implications for comparative terrestrial planetology. *Geochemistry, Geophysics, Geosystems*, 2(8), 1026. <https://doi.org/10.1029/2000GC000115>
- Royden, L., & Holt, A. F. (2020). Subduction Dynamics and Mantle Pressure: (i) An analytical framework relating Subduction Geometry, Plate Motion, and Asthenospheric Pressure. *Geochemistry, Geophysics, Geosystems*, e2020GC009032. <https://doi.org/10.1029/2020GC009032>
- Royden, L. H., & Husson, L. (2006). Trench motion, slab geometry and viscous stresses in subduction systems. *Geophysical Journal International*, 167, 881–895.
- Schellart, W. P., Freeman, J., Stegman, D. R., Moresi, L., & May, D. A. (2007). Evolution and diversity of subduction zones controlled by slab width. *Nature*, 446, 308–311.
- Schubert, G., & Turcotte, D. L. (1972). One-dimensional model of shallow mantle convection. *Journal of Geophysical Research*, 77, 945–951.
- Schubert, G., Yuen, D., Froidevaux, C., Fleitout, L., & Souriau, M. (1978). Mantle circulation with partial shallow return flow: Effects on stresses in oceanic plates and topography of the sea floor. *Journal of Geophysical Research*, 83, 745–758.
- Sharples, W., Jadamec, M. A., Moresi, L. N., & Capitanio, F. A. (2014). Overriding plate controls on subduction evolution. *Journal of Geophysical Research: Solid Earth*, 119, 6684–6704. <https://doi.org/10.1002/2014JB011163>
- Stadler, G., Gurnis, M., Burstedde, C., Wilcox, L. C., Alisic, L., & Ghosh, O. (2010). The dynamics of plate tectonics and mantle flow: From local to global scales. *Science*, 329(5995), 1033–1038.
- Stegman, D. R., Freeman, J., Schellart, W. P., Moresi, L., & May, D. (2006). Influence of trench width on subduction hinge retreat rates in 3-D models of slab rollback. *Geochemistry, Geophysics, Geosystems*, 7, Q03012. <https://doi.org/10.1029/2005GC001056>
- Steinberger, B. (2016). Topography caused by mantle density variations: Observation-based estimates and models derived from tomography and lithosphere thickness. *Geophysical Journal International*, 205, 604–621. <https://doi.org/10.1093/gji/ggw040>
- Steinberger, B., Conrad, C. P., Osei Tutu, A., & Hoggard, M. J. (2019). On the amplitude of dynamic topography at spherical harmonic degree two. *Tectonophysics*, 760, 221–228. <https://doi.org/10.1016/j.tecto.2017.11.032>
- Stevenson, D. J., & Turner, J. S. (1977). Angle of subduction. *Nature*, 270, 334–336.
- Tovich, A., Schubert, G., & Luyendyk, B. P. (1978). Mantle flow pressure and the angle of subduction: Non-Newtonian corner flows. *Journal of Geophysical Research*, 83, 5892–5898.
- Van der Meer, D. G., Hinsbergen, D. J. J., & Spakman, W. (2018). Atlas of the underworld: Slab remnants in the mantle, their sinking history, and a new outlook on lower mantle viscosity. *Tectonophysics*, 723, 309–448.
- Watkins, C. E., & Conrad, C. P. (2018). Constraints on dynamic topography from asymmetric subsidence of the mid-ocean ridges. *Earth and Planetary Science Letters*, 484, 264–275. <https://doi.org/10.1016/j.epsl.2017.12.028>
- Yamamoto, M., Phipps Morgan, J., & Morgan, W. J. (2007). Global plume-fed asthenosphere flow: (1) Motivation and model development. In G. R. Foulger, & D. Jurdy (Eds.), *Plates, Plumes, and Planetary Processes: Geological Society of America, Special Paper 430* (pp. 165–188). Boulder, CO: Geological Society of America.
- Yamato, P., Husson, L., Braun, J., Loiselet, C., & Thieulot, C. (2009). Influence of surrounding plates on 3D subduction dynamics. *Geophysical Research Letters*, 36, L07303. <https://doi.org/10.1029/2008GL036942>
- Yang, T., Moresi, L., Muller, R. D., & Gurnis, M. (2017). Oceanic residual topography agrees with mantle flow predictions at long wavelengths. *Geophysical Research Letters*, 44, 10,896–10,906. <https://doi.org/10.1002/2017GL074800>
- Zhong, S., & Gurnis, M. (1994). Controls on trench topography from dynamic models of subducted slabs. *Journal of Geophysical Research*, 99, 15,683–15,695.
- Zhong, S., Ritzwoller, M., Shapiro, N., Landuyt, W., Huang, J., & Wessel, P. (2007). Bathymetry of the Pacific Plate and its implications for thermal evolution of lithosphere and mantle dynamics. *Journal of Geophysical Research*, 112, B06412. <https://doi.org/10.1029/2006JB004628>